Universidad de La Laguna

Master Thesis

Investigation of Cold Accretion Disks in Low-Luminosity AGN: Evidence from the Sombrero Galaxy

Author:
Gonzalo Marrero Ramallo

Supervisor:
Almudena Prieto Escudero

Julio, 2024

Contents

Abstract

Los agujeros negros supermasivos (SMBH) son fenómenos astrofísicos de gran interés que se encuentran en el centro de la mayoría de las galaxias masivas en el universo observable. Estos objetos, con masas que pueden alcanzar millones o incluso miles de millones de veces la masa del Sol, desempeñan un papel fundamental en la evolución de las galaxias y en la regulación de la formación estelar en su entorno más próximo. A través de procesos de acreción de materia, los SMBH pueden generar una gran cantidad de energía y radiación, manifestándose en algunos casos como núcleos activos de galaxias (AGN).

En este estudio, se enfoca en la Galaxia de Sombrero (NGC4594), que alberga un SMBH en su centro. Se trata de un AGN denominado de baja luminosidad. Se utilizan datos observacionales de baja y muy alta resolución obtenidos por varios telescopios, que se complementan con nuevos datos del telescopio espacial James Webb (JWST), se investiga la distribución espectral de energía de este objeto y la posible existencia de un disco de acreción frío, con un enfoque específicamente en la región del Big Blue Bump en la región del óptico y UV del espectro de energía (SED), donde se espera que el disco de acreción emita una cantidad significativa de radiación que debido al polvo de nuestra propia galaxia, no podemos ver, además de por ser fuentes mucho menos luminosas que los AGNs de alta luminosidad como los quasares y galaxias Seyfert, donde la estructura de disco de acreción se ha demostrado estar presente.

Para ello se representa la SED de nuestro objeto y se ajusta con tres leyes de potencias para simular la contribución del jet y un modelo de disco de acreción truncado (Sakura-Sunyaev), de manera análoga a como se realiza en AGNs más luminosos.

Los resultados revelan nuevas perspectivas sobre los procesos de acreción en los AGN de baja luminosidad y en concreto en este estudio, se contempla con los nuevos datos de alta resolución tratados para NGC 4594, se ajustan a un disco de acreción frío; es decir desplazado hacia longitudes de onda más largas. Por tanto, este trabajo sienta un precedente en el estudio de AGNs de baja luminosidad, ya que proyecta una característica solo encontrada en objetos mucho más luminosos, y hasta el momento solo aventurada por la carencia de datos de tan alta resolución con los que se cuenta en este trabajo, los cuales desvelan esa región del espectro hasta entonces difusa para estos objetos.

1. Introduction

As it is known, black holes are fascinating and amazing phenomena that are found in various forms throughout our universe. For one hand, black holes of stellar masses are found in binary systems, where either indirect observations by investigation of their visible companion, or direct observations of their Interaction (Reb et al. 2018). For the other hand, there are strong observational evidences supporting the presence of supermassive black holes (SMBH; $M_{BH} \sim 10^6$– 10^6 $M_\odot$) in the nucleus of essentially every massive galaxy ($M_* \geq 10^{10}$ $M_\odot$) (Kormendy & Ho 2013).

Active Galactic Nuclei (AGN) are related to the main feature that distinguishes these objects from inactive (normal or regular) galaxies: the presence of supermasive accreting black holes in their centers (Netzer 2013). As it stands, central black holes (BHs) are now believed to be basic constituents of most, if not all, massive galaxies (Kormendy & Ho 2013). The realization that BH mass correlates strongly with the properties of the host galaxy has generated intense interest in linking BH growth with galaxy formation (Kormendy & Ho 2013; Ho 2008).

AGNs can be identified by a variety of methods. For example different surveys using different techiques identified the presence of strong or broad emission lines, an unusually blue continuum, or strong radio or X-ray emission. All of these methods are effective, but none is free from selection effects. To search for AGNs in nearby galaxies, where the nonstellar signal of the nucleus is expected to be weak relative to the host galaxy, the most effective and least biased method is to conduct a spectroscopic survey of a complete, optical-flux limited sample of galaxies. To be sensitive to weak emission lines, the survey must be deep and of sufficient spectral resolution. To obtain reliable line intensity ratios on which the principal nuclear classifications are based, the data must have accurate relative flux calibration, and correction for the starlight contamination (Ho 2008).

1.1. Black Holes

1.1.1. General Scheme

If we talk about black holes from a general point of view, there are numerous known stellar-sized BHs in our galactic neighborhood, and in several nearby galaxies, with masses in the range 3–30 $M_\odot$. These are the remnants of core collapse in type-II supernovae (SNe) with very massive progenitors (20 or 30 $M_\odot$). Such objects are found in binary systems that are also strong X-ray sources, probably the result of accretion onto the BH. A direct causal connection between the SN explosion and the remnant BH has been established in several cases Netzer (2013).

Active supermassive BHs, in galactic centers, have been known since the early discovery of quasars in the 1960s Netzer (2013). We know believe that quasars are cosmological objects and their large redshift represent the cosmological expansion Kato (1998). Most of the galaxies even the dormant ones, contained a central black hole. Detailed studies of the stellar velocity field and gas motion in about 60 nearby galaxies suggest the existence of such objects Netzer (2013).

Observations of active supermassive black holes reveal that these systems must have existed very early in the history of the universe. In fact, observations of AGNs at large redshift show that BHs as large as $10^9 M_\odot$ have already been in place at $z \approx 6$. Some of these sources are accreting matter at a very high rate, close to the theoretical upper limits as Eddington limit Netzer (2013).

1.1.2. General Black Hole Properties

Black Holes (BHs) are extreme cases of curved space-time and are described by general relativity theory that describe the three main properties that describe a black hole: mass, charge, and angular momentum. Some of these properties can be linked using the BH mass M and gravitational radius r_g as:

$$r_g = \frac{GM}{c^2} \tag{1}$$

$$r_g \approx 1.5 \times 10^{13} M_8 \text{ cm} \tag{2}$$

where M_8 is the BH mass in units of $10^8 M_\odot$.

It is convenient to define another parameter, a, such that $\alpha = \frac{a}{s/M} = \frac{arGc}{s/M}$. It is related to the specific angular momentum. This value can take values between -1 and 1. Several important properties of AGN BHs depend on their spin since this determines the maximum energy that can be extracted from the hole during accretion.

In the case of $a = 0$, setting $a = 0$ gives two solutions for the event horizon,

$$r_\pm = r_g \left(1 \pm \sqrt{1 - a^2}\right). \tag{3}$$

For extreme black holes with $a = 1$, the outer radius is at $r_+ = r_g$, and for $a = 0$, it is at $r_+ = 2r_g$. Besides the two event horizons, the Kerr metric also features an additional surface of interest called the static limit, given by

$$r_0 = r_g \left(1 + \sqrt{1 - a^2 \cos^2 \theta}\right). \tag{4}$$

The region of space between r_0 and r_+ is called the ergosphere. The location of the innermost stable circular orbit (ISCO), also called the marginal stability radius, r_{ms}, beyond which the particle loses its orbital motion and falls directly into the event horizon. For a Schwarzschild BH, $r_{ms} = 6r_g$, and for rotating Kerr BHs with $a > 0$, $1 \leq r_{ms} \leq 6r_g$, where the exact value depends on a.

The value of r_{ms} determines the fraction of the gravitational potential energy that is converted to electromagnetic radiation during the accretion. The smaller r_{ms} is, the larger is this fraction. For thin accretion disks, r_{ms} is taken as the innermost radius of the disk. Thick accretion disks are different, and closer orbits, so-called marginally bound orbits, can be achieved.

Given the assumption that r_{ms} is the innermost possible orbit, and using the notation $x = r/r_g$ for the normalized distance from the hole, one can solve for η, the efficiency of converting rest mass to electromagnetic radiation, due to the infall of mass m from infinity to r_{ms}. In general, $\eta = \frac{E(\infty) - E(r)}{mc^2}$. For a stable circular orbit at the ISCO, this is the equivalent of the Newtonian term $\frac{1}{2}x$. The increase in BH mass

due to the subsequent fall of this mass into the BH is $(1-\eta)m$.

The efficiency parameter η depends only on the BH properties, assuming all the gravitational energy is converted to electromagnetic radiation. There are other cases in which part of this energy is advected into the BH, thus decreasing the efficiency of the radiation process. In such cases, a different efficiency factor, η_r is used to describe the relationship between m and E_G. Obviously, $\eta_r \leq \eta$.

GR calculations show that for an ISCO at a normalized radius x, The equation for a in terms of x is given by:

$$a = \frac{x^{1/2}}{4-(3x-2)^{1/2}}. \tag{5}$$

The equivalent relationship between x and η is:

$$\eta = 1 - \sqrt{\frac{1-2/3x}{1-(3x)^{1/2}}}.s \tag{6}$$

For example, in a Schwarzschild BH with $x = 6$, $\eta = 0.057$ Netzer (2013). This value and other values can be found in 1. The present sub section 1.1.2 is based on Netzer (2013).

1.2. General accretion process in Black Holes

The accretion disk paradigm, explain that since the discovery of quasars it was proposed the situation of black hole disk accretion by Lynden-Bell. When the gas infalls on a massive object, some of the gravitational energy of the gas is released. This is call a *mass - accretion process*. In 1970 the importance of the accretion process and accretion disks began to be recognized in the field of interacting binary stars. One of these models are the Sakura - Sunyaev (standard accretion-disk model) Kato (1998). According to the Sakura Sunyaev theory, the energy is eventually transformed into radiation, so that a bright disk can be observed Shakura & Sunyaev (1973). Decades later, a new type of optically-thick disks appeared: advection-dominated slim disk. In this model, advective energy transport plays a dominant role. These models are called *advection-dominated accretion flows (ADAFs)*. This configuration is tipycally founded in AGNs Kato (1998).

A general definition of an accretion disk is a rotating gaseous disk (mainly hidrogen) with accretion flow, which form around a gravitating objects. It cause a widely variety of active phenomena in the universe such as star formation, high - energy radiation, binary evolution, novae and type I supernovae, quasars, jets, ... Kato (1998)

The simplest case of accretion is spherical. The accretion in this case starts at a large distance from the center, where the gas is at rest. When then follow the gas radial motion under the combined force of gravity and radiation pressure force.

As a result, most of the gravitational energy is advected into the central object, and the radiated luminosity is only a small fraction of the released gravitational energy. A good estimate for the luminosity of a spherical accretion event is

$$L \sim 10^{-4} \left(\frac{\dot{M}}{\dot{M}_{Edd}} \right)^2 \dot{M}_{Edd}. \tag{7}$$

In terms of radiative efficiency, this is equivalent to $\eta \sim 10^{-4}$. Although the luminosity and L/L_{Edd} in spherical accretion onto a supermassive black hole are very small compared with accretion via a disk, the actual energy produced by the process can be large Netzer (2013). For AGNs, later we will discuss the fact that the typical signature is an optically thick accretion disk, in section 1.3.6.

Finally, there are two important parameters related to accretion process are Eddington Luminosity and Eddington Accretion Rate.

1.2.1. Eddington Luminosity. Accretion Rate

If a central point source with mass M is assumed, total luminosity L, and monochromatic luminosity L_ν. Assume also fully ionized gas at a distance r from the source. The radiation pressure force acting on a gas particle is:

$$F_{rad} = \frac{N_e \sigma T}{4\pi r^2 c} \int_0^\infty L_\nu d\nu = \frac{N_e L \sigma T}{4\pi r^2 c} \tag{8}$$

where N_e is the electron density and σT is the Thomson cross section. The gravitational force per particle is:

$$F_{grav} = \frac{GM\mu m_p N_e}{r^2} \tag{9}$$

where μ is the mean molecular weight (mean number of protons and neutrons per electron; about 1.17 for a fully ionized solar composition gas). Spherical accretion of fully ionized gas onto the central object can proceed as long as $F_{grav} > F_{rad}$. The limiting requirement for accretion, $F_{rad} = F_{grav}$, leads to the definition of the Eddington luminosity,

$$L_{Edd} = \frac{4\pi c GM\mu m_p}{\sigma_T} \times 1.5 \times 10^{38} \left(\frac{M}{M_\odot} \right) \text{ ergs}^{-1} \tag{10}$$

where the factor 1.5×10^{38} depends on the exact value of μ and was calculated for solar metallicity gas. For a pure hydrogen gas, this factor is about 1.28×10^{38}. The value of L_{Edd} defined in this way is the maximum luminosity allowed for objects that are powered, over a long period of time, by a steady-state accretion. Obviously, the luminosity can exceed this limit for a short duration, for example, immediately after an outburst. Netzer (2013)

More realistic situations may involve partly neutral gas and hence much higher opacity. Here the effective L_{Edd} can be significantly smaller than the value defined in equation (10). Given the definition of L_{Edd}, and the accretion rate $\dot{M} = L/\eta c^2$, where η is, again, the mass-to-luminosity conversion efficiency, we can define several other useful quantities. The first is the Eddington accretion rate, $\dot{M}_{Edd}$, which is the accretion rate required to produce a total luminosity of L_{Edd}:

$$\dot{M}_{Edd} = \frac{L_{Edd}}{\eta c^2} \approx 3 \times 10^8 \left(\frac{M}{M_\odot}\right) \eta_{0.1}^{-1} \, M_\odot \, yr^{-1} \tag{11}$$

The normalized Eddington accretion rate,

$$\dot{m} = \frac{\dot{M}}{\dot{M}_{Edd}} = \frac{\dot{M}c^2}{\eta L_{Edd}} = \frac{\eta \dot{M} c^2}{L_{Edd}} \tag{12}$$

The $\dot{M}$ refers to the mass inflow rate into the BH and is thus the infall accretion rate. The BH growth rate is $\dot{M}(1-\eta)$ Netzer (2013).

Table 1: Properties of Schwarzschild and Kerr BHs Netzer (2013)

a	r_{ms}/r_g	η
−1.0	9.0	0.038
0	6.0	0.057
0.1	5.67	0.061
0.5	4.23	0.082
0.9	2.32	0.156
0.998	1.24	0.321
1.0	1.00	0.423

The present sub section 1.2.1 is based on Netzer (2013).

1.2.2. General Accretion Disks

As explained in section 1.2, which provides a general definition of this phenomenon, some of the most efficient accretion processes in astrophysics are associated with the presence of accretion disksKato (1998). Such disks are found in protostars; in various types of binary stars, including low- and high-mass X-ray binaries; in dwarf novae or cataclysmic variables; and in classical novae. They are also believed to be present in galactic nuclei, around the central supermassive black hole, during periods of fast accretion Netzer (2013).

Accretion disk consists mainly of hidrogen gas, helium and other elements Kato (1998).In galactic centers, accretion disks are naturally formed by infalling gas that sinks into the central plane of the galaxy while retaining most of its angular momentum. The assumption is that the viscosity in the disk is sufficient to provide the necessary mechanism to transfer outward the angular momentum of the gas and to allow it to spiral into the center, losing a considerable fraction of its gravitational energy on the way. The energy lost in the process can be converted into electromagnetic radiation with extremely high efficiency. It can also be converted to kinetic energy of gas, which is blown away from the disk, or in other cases, it can heat the gas to very high temperatures, which causes much of the energy to be advected into the BH Netzer (2013). For AGNs and LLAGNs, we will discussed the different mechanisms proccess for accreting material, in the section 1.3.6.

A standard accretion disk is flat (geometrically thin) and opaque (optically thick). The gas rotates around

the central object with different velocities at different radii. The gravitational force is balanced by the centrifugal force. Therefore, the angular speed Ω is faster in the inner regions and slower in the outer regions, according to:

$$\Omega = \sqrt{\frac{GM}{r^3}} \tag{13}$$

The friction or viscosity between the adjacent gas layers transfers angular momentum due to the viscous interaction between the inner and outer layers: the faster´s loses angular momentum and the slower´s gains momentuum. So that, the rotating disk gas gradually infalls (accretes) toward the center, whereas angular momentum is trasfered toward the outer region. Then, the standard accretion disk has an inner edge, as we explain at sub-section 1.1.2 Kato (1998).

Moreover, just a reminder, some of the basic parameters of accretion disk in general, are the mass of the object M, the mass accretion rate $\dot{M}$, and the viscous parameter α. Viscous parameter is related to the angular momentum (a parameter), as we see in section 1.1.2. The mass - accretion rate means the amount of gas that infalls to the central object per unit of time and the viscous parameter represents the magnitude of friction between the gas layers Kato (1998).

Regarding the spectrum of the standard disk, since the gravitational potential is deep at the center and the rotation speed is fast there, the heating rate is also larger in the inner region than in the outer one. Futhermore, the gas temperature of the disk is higher in the inner region. The gas is assumed to radiate locally a blackbody spectrum with an effective temperature there. The disk has different temperatures at different radii (multi temperature), the resultant disk spectrum is a superposition of the blackbody spectra with a wide range of effective temperatures. The spectrum is called a disk blackbody Kato (1998). See figure 1.

1.3. Active Galactic Nuclei

The central region of some galaxies emits large amounts of radiation across basically the whole electromagnetic spectrum, from radio to gamma-rays, sometimes with high luminosities of up to $L_{bol} \approx 10^{47}$ erg s^{-1}; these regions are called Active Galactic Nuclei (AGN), and the galaxies that host them are therefore called active galaxies. The observed radiation comes from a compact, spatially unresolved region where matter is being accreted onto a supermassive black hole López (2021).

The release of gravitational energy of matter falling deep into the gravitational potential of a very compact body as a black hole, can be far more efficient. In the last decades the cientific consensus evolved subsequently and led to the current picture of AGNs: At the centre there is likely a supermassive black hole accreting matter Reb et al. (2018). Gravitational energy release ultimately supplies all forms of radiation and outflows of the AGN Shakura & Sunyaev (1973).

Release of gravitational potential energy into head and radiation is conneted with accretion flow. This is commonly assumed to take place through a thin accretion disc as we see in section 1.2 Because of its angular momentum, the infalling gas naturally tends to accumulate in a plane. Viscosity is the key element of this disc: it allows the gas to transfer outwards its net angular momentum so that it can spiral into the central BH López (2021)

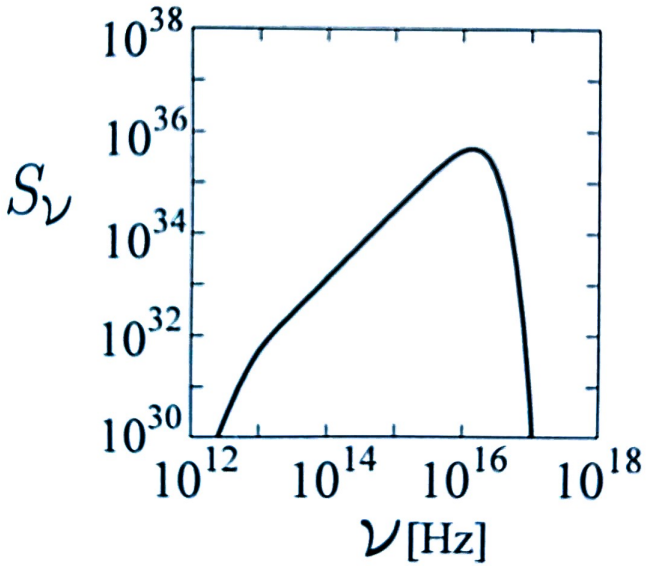

Figure 1: Spectrum of standard disk, The abcisa is the frecuency ν, while the ordinate is the intensity S_ν. In this case the parameters are for a typical case of quasars: M = $10^8 \cdot M_\odot$ and $\dot{M}$ = 1 $M_\odot \cdot yr^{-1}$ Kato (1998)

.

In this process, a considerable fraction of the gas gravitational energy is converted into radiation (especially in the optical and UV range), while the rest is converted into kinetic energy or heat.

Apart from thermal radiation associated with a disc, many AGN also exhibit non-thermal emission. Radio and high-energy fluxes are dominated respectively by synchrotron emission and inverse Compton, which are associated with relativistic outflows of collimated plasma (jets) ejected along the axis of the system and with the energy distribution of particles in the BH corona. López (2021). So, just for context, the main types of AGNs are Kato (1998):

- **Quasars.** The powerful and luminous AGN, they show star-like appearance and broad emission features with large redshifts. Typical luminosity is 10^{46-47} erg/s.
- **Radio galaxies.** The are those which radiate a huge amount of energy (10^{60} erg/s at radio wavelengths).
- **Seyfert galaxies.** These galaxies have bright compact nuclei and exhibit broad emission features. The typical luminosity is 10^{43-45} erg/s. There are two classes: type I and II. Nowadays is clear that the difference between them is supposed to be the orientation effect.
- **Low - Ionization Nuclear Emission-line Regions (LINERs).** In this case, show relatively strong lines of low - ionization species (OI or SII), from their nuclei.
- **Starburst Galaxies.** Are galaxies where star formation takes place at a high rate.
- **Low - Luminosity AGN (LLAGNs**). Are AGNs with their luminosity is quite small.

1.3.1. Unified Scheme for AGNs

According to the unified scheme Antonucci (1993); Urry & Padovani (1995), illustrated in Figure 2, AGNs typically have a number of components in common:

- Supermassive black hole in the center
- Accretion disc around the supermassive black hole
- Broad line region (BLR) in vicinity of the accretion disc
- Torus confining the inner central region
- Narrow line region (NLR)
- Jet emanating from the central region

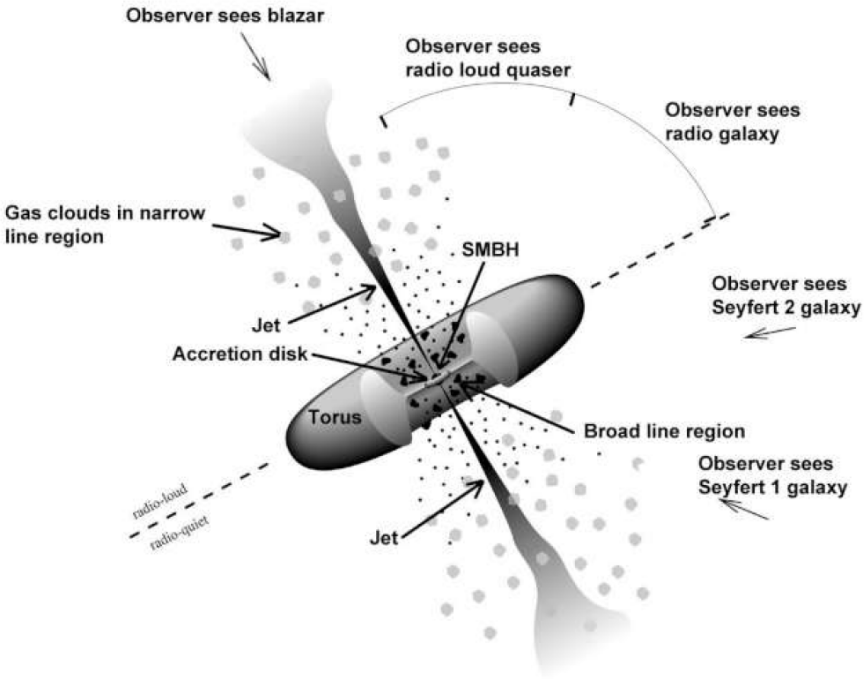

Figure 2: An unified scheme for AGN. Urry & Padovani (1995)

As it is explained in section 1.1.2 a characteristic physical scale in AGNs is its gravitational radius in equation 1. Moreover, about the accretion disk, mattercollapsing onto the black hole settles into a geometrically in a disc, due to gravity and conservation of angular momentum (geometrically thin and optically thick disk) Shakura & Sunyaev (1973). The accretion disc gives rise to a multi-temperature black body spectrum, contributing especially in the ultraviolet (UV) - the so-called blue bump Reb et al. (2018).

Above and below the accretion disc there are quickly moving gas clouds, due to their proximity to the black hole (10^{16} cm–10^{18} cm) Peterson & Ferland (1997), forming the BLR. Outside the accretion disc and the BLR, a dusty, clumpy, gaseous torus of typically parsec-scale size ($\approx 10^{17}$ cm) surrounds the central region, presumably with similar orientation as the disc. The material shields radiation from the inner region and gives rise to thermal emission in the infrared (IR). Finally, AGN jets are formed through interactions between surrounding material and intense magnetic fields near the central black hole: they are collimated streams of relativistic particles extending from the central region to significant distances. These jets, ranging from parsecs to kiloparsecs in length, play a crucial role in modulating star formation activity and in the evolution of host galaxies by depositing large amounts of energy into their surroundings in a process known as feedback Reb et al. (2018).

The basic idea is to locally convert a fraction of the released gravitational potential energy into black body radiation Kato (1998). A viscosity prescription results in torques, which transport angular momentum outwards. That enables matter to spiral further in, providing the mass supply for the AGN Reb et al. (2018).

An important quantity connected to accretion is the Eddington limit, as we see in equation 10 which is the maximum luminosity L_{Edd} a source of mass M can emit as we see in sub section 1.2.1. It is common to express the luminosity of AGNs in terms of the Eddington luminosity Reb et al. (2018).

1.3.2. General Properties

AGNs spend their lives in low state. They derive their energy output from BH accretion implies the presence of a SMBH (Super Massive Black Hole) in the host galaxy Ho (2008). AGNs are luminous compared with normal galaxies. In some cases the luminosity is up to 10^{12-13} $L_{\odot}$ Kato (1998). They can be identified by the presence of strong or broad emission lines or strong radio or X- ray emission Ho (2008).

The luminosity of AGNs is believed to have non-stellar origins Kato (1998). So sensitivity to weak emission lines required sufficient spectral resolution as it was claimed in this present work. A harder radiation field, as an AGN power-law continuum that extend into the extrem UV and X-ray penetrates much deeper into an optically thick cloud, creating a partially ionized zone and strong low - ionization forbidden lines. Hard AGN radiation field also boosts the production of collisionally excited forbidden line emission because its high termal energy Ho (2008).

In some cases, the evidence of a SMBH (Super Massive Black Hole) is estimated by means of the stellar distribution or stellar velocity dispersion. In other cases, the gas motion in the central region based on emission-line spectroscopy, provided a guess as to the mass of the black hole. Following the last idea, classical AGN spectrum consits of the UV blue-bump and power law spectrum. These properties can never be reproduced by superpositions of any stellar spectra. This spectrum are usually interpreted as spectra from optically-thick accretion disk and so that, an strong evidence of it. Kato (1998).

Spectroscopy evidence of accretion disks was found as an asymetric double-peaked profiles for Balmer emission lines Chen & Halpern (1989b). Also, AGNs vary their brightness on short timescales ranging from a few days or minutes to years. This means that some sort of activity takes place in a very compact central region. They have a peculiar appearance such bursts of central regions, radio lobes and jets. Finally,

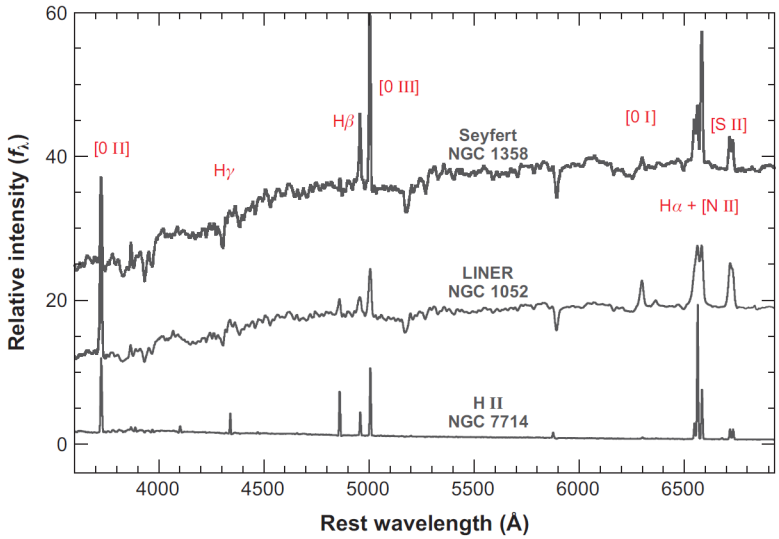

Figure 3: Sample optical spectra of the various classes of emission-line nuclei. Prominent emission lines are identified. The ionization level can be judged by the relative strengths of the oxygen lines, but in practice it can be solved by the [O III]/Hβ ratio. In the commonly adopted system of Veilleux & Osterbrock (1987), the division between Seyferts and LINERs occurs at [O III]λ5007/Hβ = 3.0 Veilleux & Osterbrock (1987). Ho (2008)

sometimes they exhibit relativistic phenomena, such as superluminical motions of radio blobs and high energy particle emission Kato (1998).

1.3.3. Nuclear Properties

AGNs are nuclear sources with power-law spectra at optical and UV wavelenghts described by a continuum density as $f_\nu \propto \nu^\alpha$, with $\alpha \approx -0.5$ Vanden Berk et al. (2001). This continuum traces the low-frequency tail of the "big blue bump" Shields (1978), which supplies the bulk of the ionizing photons. This feature is extremely difficult to detect in LLAGNs, both because the big blue bump is weak or absent and sources are faint. Optical nuclei of LINERs can be 10^{14} times fainter than their host. To solve this problem, it should be interesting to explore nuclear point sources in the optical and near-IR. The most robust technique to extract faint nuclei in the presence of some complications such as the point spread function or stellar contamination, employs two-dimensional multicomponent fitting Ho (2008). Dust obscuration is probabily the main reason for the non detection of UV emission in the majority of LINERs Pogge et al. (2000).

For other hand, AGNs, no matter how weak, are almost never silent in the radio. The presence of a compact radio core is therefore a good AGN indicator. Radio emission in LINERs is confined to a compact core or base of a jet Ho (2008).

Some properties for X - ray cores in AGNs are:

- **Region of ~0.5–10 keV.** Over this region, the continuum can be fit with a power-law with an energy index of $\alpha \approx -0.4$ to -1.2. Although this range overlaps with that seen in more luminous sources, the typical value of ~ -0.8 in LLAGNs may be marginally flatter than in Seyfert Ho (2008)

- **Power-law component.** This component shows very little intrinsic absorption. This trend conflicts with the tendency for the degree of obscuration to increase with decreasing luminosity Lawrence & Elvis (1982)

- **Fe- Kα emission.** Signatures of X-ray reprocessing by material from an optically thick accretion disk, in the form of Fe Kα emission or Compton reflection are weak or absent; the weakness of the Fe Kα line in LLAGNs runs counter to the inverse correlation between iron line strength and luminosity observed in higher luminosity AGNs. In the few cases where Fe Kα emission has been detected, it is always narrow Ho (2008).

- **Thermal Plasma Model.** Apart from the hard power-law, most objects require an extra soft component at energies of ~2 keV that can be fit by a thermal plasma model. Contrary to the trend established for luminous sources, short-term, large-amplitude X-ray variability is rare in LLAGNs Ptak et al. (1998)

About the circumnuclear plasma, their origin it is still on debate. Without better resolution it is complicated to determinate how much of the gas is truly associated with the nuclear region of the galaxy, or the density and temperature profile Ho (2008). An starburst origin is an improbable scenario González-Martín et al. (2006). Furthermore, high-resolution spectroscopy of the highly ionized gas around the nucleus of M81, reveals that plasma is collisionally ionized Starling et al. (2005); this may be a property unique to LINERs: as thermal gas in luminous Seyferts is usually photoionized rather than collisionally ionized Kinkhabwala et al. (2002)

Referring to the Broad Line Region (BLR), AGNs are distinguished by their characteristic broad permitted lines. The broad component becomes progressively more difficult to detect in ground-based spectra for permitted lines weaker than Hα Ho (2008). Some LINERs contain broad lines with double-peaked profiles: they are often interpreted as a kinematic signature of a relativistic accretion disk Chen & Halpern (1989a).

Double-peaked broad-line AGNs may be more common than previously thought, especially among LLAGNs, perhaps as a consequence of their accretion disk structure.What fraction of the more numerous LINER 2s are AGNs? LINERs of either type generally show very little sign of absorbing or reprocessing material, and UV variability is common. An excellent example of a LINER with a naked type 2 nucleus is the Sombrero galaxy that shows no trace of a broad-line component purposes; the continuum emission from the nucleus looks unobscured Ho (2008)

Fe Kα emission is expected from reprocessed material, and this is consistent with the modest mid-IR emission Bendo et al. (2006) So it appears that there is no sign of BLR so, where is the BLR? It is just not there. The lack of a BLR in very low-luminosity sources may be related to a physical upper limit in the broad-line width Laor (2003). If LLAGNs obey the same BLR-luminosity relation as in higher luminosity systems, their BLR velocity depends on the BH mass and luminosity.

The BLR originates from a disk outflow formed at the transition radius between regions dominated by gas and radiation pressure. As this radius shrinks with decreasing L_{bol}/L_{Edd}, where $L_{Edd} = 1.3\times10^{38}(M_{BH}/M_{\odot})$ ergs s^{-1}, the BLR is expected to disappear for $L_{bol}/L_{Edd} \lesssim 10^{-3}$. The apparent correlation between BLR line width and L_{bol}/L_{Edd} Ho (2008) suports this situation. So, LINERs generally lack UV resonance absorption

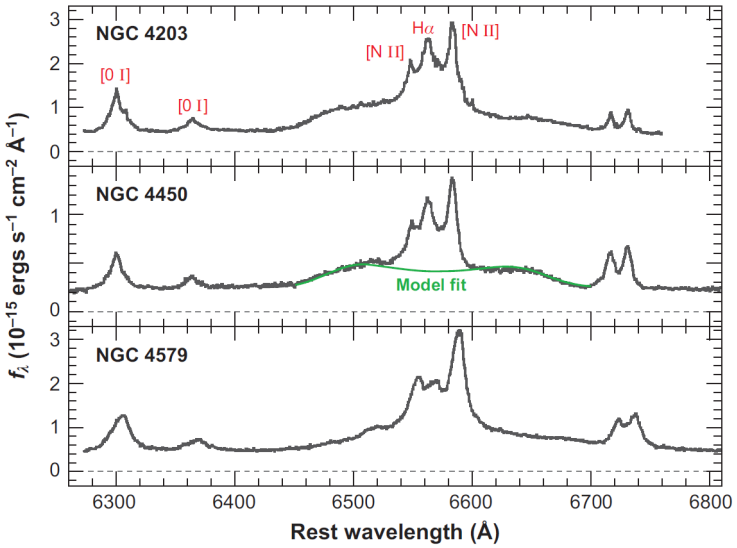

Figure 4: Sample spectra of three classes of LINERs with double-peaked Hα, discovered with the Hubble Space Telescope. A model fit for the disk profile in NGC 4450 is shown for illustration (smooth green curve). Adapted from Ho et al. (2000); Shields et al. (2000); Barth et al. (2001)

features indicative of nuclear outflows Shields et al. (2002). Several researchers have raised the suspicion that LINER 2s may not be accretion-powered.

Just to clarify regarding LINERs, we have identified two distinct classes. LINERs 1, show emission lines of high ionization as [O III] or [He II], very typical of active AGNs such as quasars and Seyfert 1. The presence of these high ionization lines is an strong evidence of an active AGN with a SMBH in its center: they emit intense radiation and an accretion disk appears too. They show as well, low ionization lines. However, LINERs 2, only show low-ionization lines. No evidence of any high-ionization lines in this cases. The abscense of high-ionization lines in this type of LINERs suggest that the activity of the nuclei is weaker than LINERs 1. The source of ionization of LINERs 2 is vary: from stellar radiation to stellar formation.

LINER 2s have a lower $L_X/L_{H\alpha}$ ratio than LINER 1s Ho & Peng (2001). In particular, the observed X-ray luminosity from the nucleus, when extrapolated to the UV, does not have enough ionizing photons to power the Hα emission Terashima et al. (2000).

So, there are three posibilities:

- X-rays are heavily absorbed.
- Non-nuclear processes power much of the optical line emission.
- Ionizing spectral energy distribution (SED) is different than assumed.

A final conclussion of this is that the AGN fraction among LINER 2s is at least 60 % and maybe as high as 100 %.

In line with the absence of a BLR discussed above and using very much the same set of evidence, torus also disappears at very low luminosities. In a large fraction of nearby LINERs, undetected Fe Kα emission indicate that we have a unobstructed view of the nucleus Ho (2008).

Finally, the kinematics of the NLR are complex. The velocity widths of the ionized gas in the LINER nuclei of early-type galaxies can be modeled as unresolved rotation of a thin disk in the gravitational potential of the central BH Verdoes Kleijn et al. (2006). Also, the velocity fields are generally disorganized, rarely showing clean signatures of dynamically cold disks undergoing circular rotation Ho (2002). Futhermore, above a certain luminosity threshold—one that perhaps coincides with the LINER/Seyfert division—AGN outflows and radio jets strongly perturb the kinematics of the NLR Walsh (2011).

It is possible as central AGN injects a source of dynamical heating of nongravitational origin to the NLR, either in the form of radiation pressure from the central continuum or mechanical interaction from radio jets, which have an important role Ho (2008).

1.3.4. Spectral Energy Distribution

The broad-band SED provides one of the most fundamental probes of the physical processes in AGNs. Both thermal and nonthermal emission contribute to the broad-band spectrum of luminous AGNs such as quasars and classical Seyfert galaxies Ho (2008).

The SED can be separated into three diferent components:

- Radio synchrotron emission from a jet. Could be strong (radio-loud) or weak (radio-quiet) Elvis et al. (1994)
- IR excess, which is considered to be predominantly thermal reradiation by dust grains Ho (2008)
- Prominent optical to UV “big blue bump" that is interpreted to be as a pseudoblackbody emission from an optically thick, geometrically thin accretion disk Shields (1978)
- Soft X-ray excess, whose origin is still highly controversial Done et al. (2007)
- A power-law, which is most conspicuous at hard X-ray energies but is thought to extend down to IR wavelengths, that can be attributed to Comptonization of softer seed photons Ho (2008).

So, LINERs may possess a weak UV continuum was made in the context of double-peaked broad-line AGNs Chen & Halpern (1989b) or SEDs are flat in the far-IR Halpern & Eracleous (1994). Other authors proposed that the relative weakness of the UV continuum compared to the X-rays is a consequence of a change in the structure of the central accretion flow, from a standard thin disk to an ion-supported torus Petre et al. (1993).

The complete extent of the distinctive spectral characteristics of Low-Luminosity Active Galactic Nuclei (LLAGNs) is still incomplete; it requires multiwavelength data. Some investigations focused on individual LLAGNs, highlighting features such as the faintness of the UV bump (Sombrero Galaxy, Nicholson et al. (1998)) and the overall agreement of the Spectral Energy Distribution (SED) with spectral models derived

from advection-dominated accretion flows (ADAFs, Yuan (2007). These findings provide solid proof of the existence of these systems at low Eddington ratios.

There are two regimens, related to the Eddington ratio: $L_{bol}/L_{Edd} = 0.1$ to 1, typical of classical, luminous AGNs, and $L_{bol}/L_{Edd} < 10^{-3.0}$, which characterizes most nearby LLAGNs. Some of them shared the main characteristics of LINER SED as:

- The big blue bump is absent Ho (2008).
- A broad excess is shifted to the mid-IR, forming a "big red bump". This component is probably related to the mid-IR excess Chen & Halpern (1989a).
- As a consequence of this shift, the optical-UV slope is exceptionally steep, generally in the range $\alpha_{ou} \approx -1$ to -2.5, to be compared with $\alpha_{ou} \approx -0.5$ to -0.7 for luminous AGNs Vanden Berk et al. (2001). X-ray–to–optical ratio is large, resulting in $\alpha_{ox} \gtrsim -1$ Ho (2008)
- There is no evidence for a soft X-ray excess Ho (2008).
- The overall SED can be considered radio-loud Ho (2008).

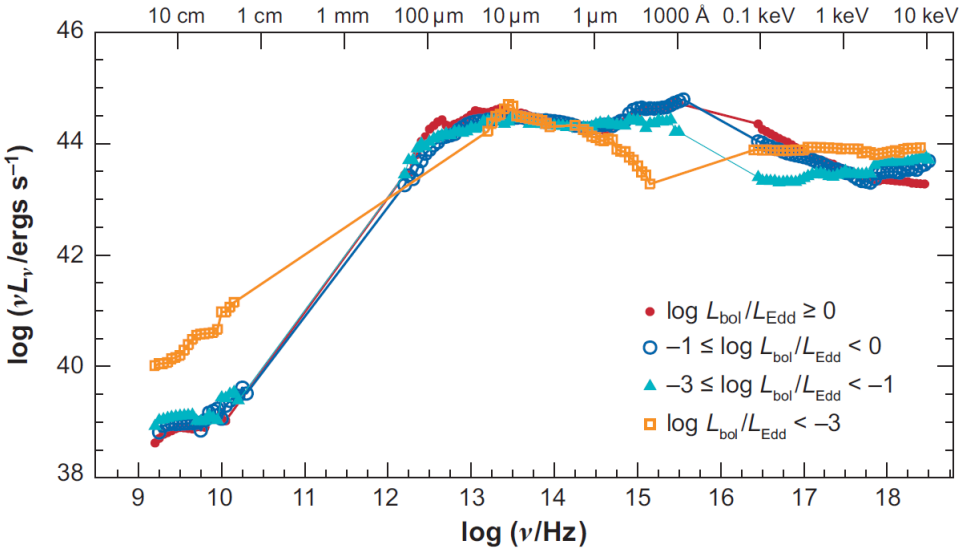

Figure 5: A diagram of a composited SED for radio-quiet AGNs binned by Eddington ratio. The SED are normalized at 1 μm. Ho (2008). For luminosity candidates, the Big Blue Bump is visible between 14 and 16 Hz. However, for LLAGNs (depicted in orange), this feature is absent.

According to this figure 5, LINERs could have very similar accretion disks compared to powerful AGNs Maoz (2007). In our results and discussion, we will delve deeper into this idea.

1.3.5. Excitation Mechanisms

The primary mechanism proposed for exciting LINERs is photoionization by a central AGN, akin to models used to elucidate brighter sources. This stems from the growing recognition of the ubiquity of black holes and the capacity of these models to elucidate observed features in LINERs by fine-tuning the ionization parameter. Despite the intuitive appeal of AGN photoionization, alternative excitation mechanisms for LINERs have been proposed.

Collisional ionization by shocks has emerged as a prominent contender. However, a challenge with this theory is reconciling the anticipated higher excitation spectrum produced by shocked gas, particularly in the UV, compared to photoionized gas. Understanding the interplay between shocks and photoionization is vital for gaining insights into the underlying physical processes. Another proposed model involves hot stars generated in short-duration bursts of star formation as the primary source of ionizing photons. However, typical O-type stars found in galactic disks do not emit sufficiently strong low-ionization lines to explain LINER spectra, although conditions in galactic centers may be more conducive to LINER-like spectra.

There are several potential explanations for the observed ionization deficit. Firstly, X-rays may be heavily obscured, possibly Compton-thick, resulting in a reduction in X-rays rather than an enhancement of Hα due to absorption. Secondly, the spectral energy distribution (SED) could differ significantly, particularly with a more pronounced UV component. However, this is unlikely as LLAGNs typically lack a UV bump in their SEDs. Alternatively, a substantial portion of the ionization for the narrow-line gas could originate from nonnuclear sources. Various candidates include hot, evolved stars, turbulent mixing layers, diffuse X-ray-emitting plasma, low-mass X-ray binaries (XRBs), cosmic ray heating, and mechanical heating from radio jets. Since multiple sources likely contribute, identifying the dominant mechanism requires further investigation.

The present subsection 1.3.5 is based on Ho (2008).

1.3.6. Low Luminosity AGN

Despite their low luminosity (with $L_{bol} \lesssim 10^{42}$ erg/s and $L_{bol}/L_{Edd} \lesssim 10^{-3}$), the Low-Luminosity AGNs (LLAGNs) are considered key objects within the diverse range of AGNs. While AGNs attract attention during their quasar state for short intervals in their life, they primarily exist in low-activity states for most of their duration. In fact, the majority of nearby galaxies hosting AGNs harbor LLAGNs, constituting approximately one-third of all galaxies in the Local Universe Ho (2008).

LLAGNs (Low Luminosity AGN) include active galactic nuclei with lower luminosities than the most powerful AGNs such as Quasars or Seyferts. This classification is based on luminosity. On the other hand, LINERs (Low-Ionization Nuclear Emission-Line Regions) refer to regions in the nuclei of galaxies that exhibit low-ionization lines. This classification is based on the spectrum. While some LLAGNs may be classified as LINERs due to their low ionization, not all LINERs are necessarily LLAGNs. For simplicity in this work, we use 'LINER' and 'LLAGN' interchangeably as the same category.

The strongest optical emission lines in the spectrum of LINERs include [O III] λ5007, [O II] λ3727, [O I] λ6300, [N II] λ6584, and hydrogen Balmer lines. Another candidates for low ionization lines are [Ne I],

Ne [II]. All these lines are prominent also in high-ionization AGNs, but in LINERs, their relative intensities indicate a lower mean ionization state. For example, the [O III] λ5007/Hβ line ratio in LINERs is 3–5 times smaller than in high-ionization type-II AGNs. Line diagnostic diagrams are efficient tools to separate LINERs from high-ionization AGNs Netzer (2013).

AGN disks, and accretion disks in general, are classified according to their shape into thin, slim, and thick disks. Each one of these can be optically thin or thick, depending on the column density (or surface density) and the level of ionization of the gas. The optical depth of AGN disks, during periods of fast accretion, is very large. The disks that receive most attention are optically thick, geometrically thin accretion disks Netzer (2013).

Weak nuclear activity seen in the majority of nearby galaxies traces low-level BH accretion to the more familiar form observed in powerful AGNs. So, LLAGNs are not simply scaled-down versions of their more luminous cousins. They are qualitatively different. They have three components: Ho (2008):

- **Radiatively inefficient accretion flow**. It is said that the amount of material available for accretion is small, resulting in mass accretion rates that fall far below $10^{-2}\dot{M}_{\rm Edd}$. In such a regime, the low-density, material is optically thin and cannot cool efficiently. Rather than settling into a classic optically thick, geometrically thin, radiatively efficient disk (the normal configuration for luminous AGNs) the accretion results in a radiatively inefficient distribution, whose dynamics may be dominated by advection, convection, or outflows (See figure 6). The great disparity between the available fuel supply and the actually observed accretion luminosity demands that the radiative efficiency of the accretion flow be much less than $\eta = 0.1$. Additional support for RIAFs comes from considerations of the SED, particularly the absence of the big blue bump, a classic signature of the thin disk, and the preponderance of hard X-ray spectra Ho (2008).

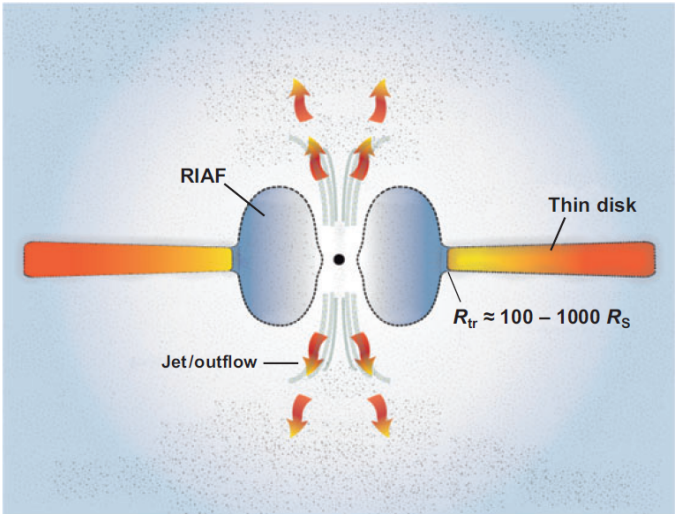

Figure 6: A diagram of the central engine of LLAGNs, consisting of three components: an inner, radiatively inefficient accretion flow (RIAF); an outer, truncated thin disk; and a jet or outflow Ho (2008)

- **Truncated thin disk**. Beyond a transition radius $R_{tr} \approx 100 - 1000 R_S$, the RIAF switches to a truncated optically thick, geometrically thin disk. The observational evidence for this component comes in three forms. First, the SEDs of some well-studied LLAGNs require a truncated thin disk to explain the big red bump—the prominent mid-IR peak and the steep fall-off of the spectrum in the optical–UV region. The thermal disk emission is cool (red) not only because of a low accretion rate but also because the inner radius of the disk does not extend all the way in to a few R_S as in luminous AGNs Lawrence (2005). Second, the very same truncated disk structure employed to model the SED simultaneously accounts for the relativistically broadened, double-peaked emission-line profiles observed in some sources. It is suggested that double-peaked broad emission lines are commonplace in LLAGNs Ho et al. (2000). The striking absence of broad Fe Kα emission in the X-ray spectra of LLAGNs, a feature commonly attributed to X-ray fluorescence off of a cold accretion disk strongly suggests that in low-luminosity sources such a structure is either absent or truncated interior to some radius, such that it subtends a significantly smaller solid angle Ho (2008).

- **Jet/Outflow**. The empirical connection between LLAGNs and jets has been established unequivocally from radio observations. From a theoretical point of view, jets may share a close physical connection with RIAFs. Thus they have a strong tendency to drive bipolar outflows owing to the high thermal energy content of the hot gas Narayan & Yi (1995). Also they may be additionally conducive to jet formation because their vertically thick structure enhances the large-scale poloidal component of the magnetic field, which plays a critical role in launching jets Livio et al. (1999).

At a qualitative level, at least, the general idea that the thin disk precedes to larger and larger radii as the accretion rate drops is probably correct Ho (2008). In an analysis of a variety of quasars with Fe Kα emission detected in XMM-Newton spectra, Inoue et al. (2007), find that the iron line profile varies systematically with Eddington ratio. Specifically, the Fe Kα profile becomes narrower with decreasing L_{bol}/L_{Edd}, a result that can be interpreted as a systematic increase in the inner radius of the accretion disk at low accretion rates.

The overall weakness of the UV continuum in Arp 102B Halpern et al. (1996) further corroborates a truncated thin disk structure and potentially provides an explanation for the low-ionization state of the emission-line spectrum. As for the jet component, it was assumed to be present, at least implicitly, insofar as the double-peaked broad-line AGNs were thought to reside preferentially in radio-loud AGNs, and the very concept of ion-supported tori was invented with reference to radio galaxies Rees (1982).

The mid-IR peak in most objects is dominated by thermal emission from the truncated thin disk rather than by the synchrotron peak of the RIAF. Second, the jet component, which was once regarded as somewhat incidental, has emerged as a natural and perhaps inevitable outgrowth of the inner accretion flow itself. Third, although the original model was invented to explain a small minority of the AGN population (double-peaked radio-loud sources), now we have good reason to believe that similar physical conditions prevail in LINERs as a class Ho et al. (2000).

1.4. Aim of this work

In the present work, we aim to address some open questions regarding LLAGNs and LINERs, focusing on the possibility of detecting a cold accretion disk. To achieve this, we will analyze the SED of the Sombrero Galaxy (NGC 4594), a candidate LLAGN and LINER.

First, we will provide some information about the Sombrero Galaxy. Then, we will establish the initial dataset that we have about our candidate. Furthermore, we will complement the results generated from the SED of the Sombrero Galaxy, focusing on the flux density values measured from several JWST data files using the MIRI and NIRSpec instruments, as well as ALMA data in the submillimeter region and VLBI data in radio.

We will fit the Sombrero data with the three broken power law corresponding to jet emission and the pseudo blackbody model typically used for the accretion disk (Shakura-Sunyaev). Once we have the model-adjusted results, we will discuss them in the context of existing literature, particularly regarding jet fits and the potential for our data to fit the accretion disk model as well as other models like ADAF. Finally, we will draw conclusions about the possibility of a cold accretion disk, which would be shifted to longer wavelengths compared to more luminous objects like quasars or Seyferts.

2. Methodology

Here, we are going to develop the method which it will be aplied to achieve the SED of Sombrero galaxy from explaining the main characteristics of Sombrero 2.1, then the dataset and high resolution data of our sample 2.3, analysis of our high resolution data of JWST of instruments NIRS 2.3.1 and MIRI 2.3.2 , some data from other telescopes such as ALMA 2.4.1 or VLBI 2.4.2, and finally how the data is fitted with the model 2.5.

2.1. Sombrero Galaxy

The sample studied in this work consists of study one of the nearby LLAGN which is also a LINER.

NGC 4594 (M104, the "Sombrero" galaxy) is a highly inclined, luminous Sa galaxy. Its distance is 9.08 Mpc (Jensen et al. 2003). The nucleus was identified as a LINER Heckman (1980). Observations using the Very Large Array find that the radio emission from NGC 4594 has three components. The central component is a compact core source (1 pc) with a flat spectrum (Hummel et al. 1984) and a variable continuum (Bajaja et al. 1988). These properties are consistent with an accretion model in which the central source derives its power from a central massive object (Hummel et al. 1984). This model is further strengthened by HST spectroscopic evidence for a $10^9 M_\odot$ black hole at the nucleus (Halpern et al. 1996).

NGC 4594 contains a stellar disc with approximately exponential brightness distribution van Houten (1961), while the optical structure of the large bulge resembles that of a giant elliptical galaxy Faber et al. (1977).

This allows the availability of high-angular resolution data from the HST in the optical range, and using adaptive optics and diffraction-limited imaging in the IR López (2021).

Name	Type	Class	z	D [Mpc]	FWHM [pc]	1″ [pc]	A_V [mag]
NGC 4594 (M104)	LINER 2	SA(s)a	0.003416	9.08	3.1	44.0	0.140

Table 2: NGC 4594 "Sombrero Galaxy" main data: Type and class are obtained by the sources describe above. The Distance and the reedshift is from Jensen et al. (2003). The spatial resolution is estimated as the FWHM of the most compact object found in the FOV. In all cases, the Galactic extinction has been corrected using the reddening values from Schlafly & Finkbeiner (2011) and the extinction curve from Chen & Halpern (1989b).

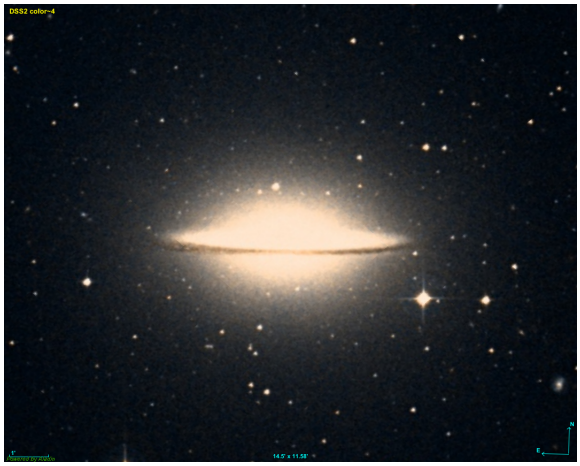

(a) A picture of Sombrero Galaxy obtained using Aladin tool, in SDSS (Sloan Digital Sky Survey) DSS2 color 14.50 arcmin x 11.52 arcmin. Optical range.

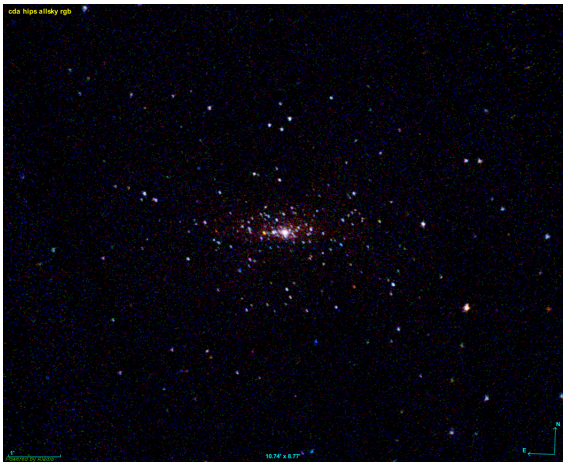

(b) A picture of Sombrero Galaxy obtained using Aladin tool, in Xandra. FoV : 10.74 arcmin x 8.77 arcmin. X-Ray range.

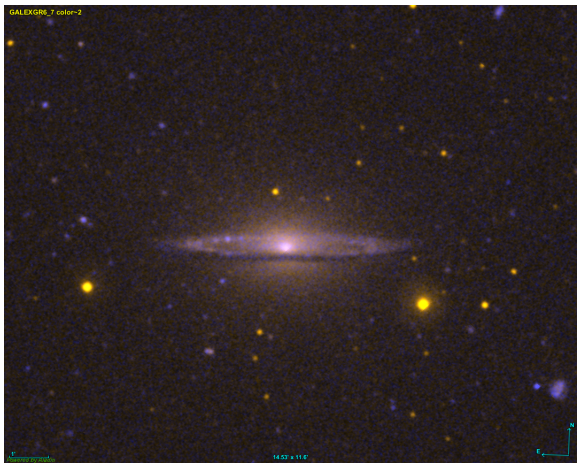

(c) A picture of Sombrero Galaxy obtained using Aladin tool, in Galex. FoV : 14.53 x 11.60 arcmin. UV range.

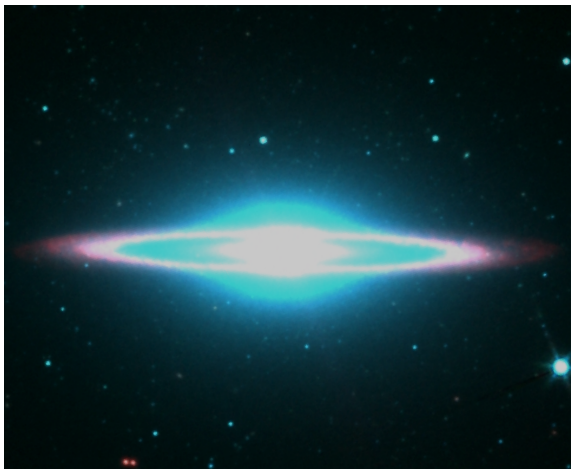

(d) A picture of Sombrero Galaxy obtained using Aladin tool, in Spitzer. FoV : 11.54 x 11.54 arcmin. IR range.

Figure 7: Images of Sombrero Galaxy in different wavelengths.

2.2. Initial dataset and High Angular Resolution SED

As it was describe in previous works, LLAGN are commonly outshined by their host galaxy Ho (2008). Therefore, very high-angular resolution datasets are needed in order to efficiently probe only the nuclear region and avoid as much contamination as possible from stellar activity, as we can see in figure 8.

For other hand, there are differences between the high and low resolution data sets, especially in the visible/UV range, where the low resolution flux is about 2 orders of magnitude larger. Apart from this, we are especially interested in the ionising part of the spectrum ($\lambda < 911$ Å), our datasets must include observations across the whole electromagnetic spectrum whenever possible, in order to have a general picture of the mechanisms going on at these nuclei López (2021).

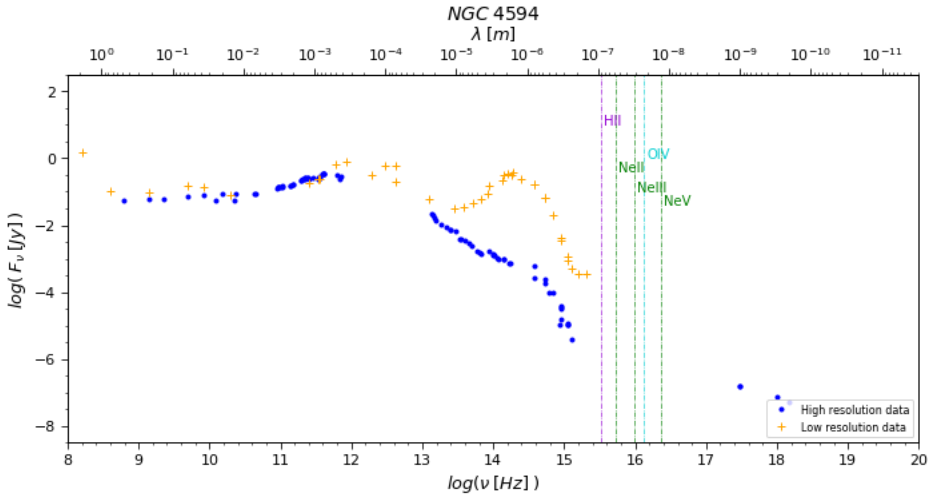

Figure 8: A Spectral flux distribution for the nucleus of NGC 4594. High and low-angular resolution data are represented by blue dots and orange crosses respectively. Vertical coloured lines are drawn at the ionisation potential of some representative species. *(This work).*

Just to provide some context about the origin of the data, we organized it from longer to shorter wavelengths and explained how we complemented the current data with our new research:

- **Radio and microwave:** From the Very Large Array (VLA), the Very Long Baseline Interferometry (VLBI), and the Atacama Large Millimeter/submillimeter Array (ALMA). The high baselines allowed by these interferometers provide some of the highest spatial resolution (≈ 0.1") López (2021) Also we complemented this data from another data from ALMA, provided by Timothy Davis in the submilimetric region between 90 GHz and 412 GHz, taking at the same time as the JWST high resolution data. Also, we complement with some VLBI (radio) data that we include in our discussion.

- **Infrarred:** In the IR, we include observations that use adaptive optics in the near-IR (NACO) and diffraction-limited imaging in the mid-IR (VISIR). Both these instruments are part of the Very Large Telescope (VLT) and also provide sub-arcsec (≈ 0.4") resolution López (2021) For other hand, we

include recent JWST data in the mid-IR with very high resolution data provided from the instruments NIRS (1.75 to 5.15 microns) and MIRI (5.00 to 28.00 microns) approximately. In the next subsection we explain how we obtain the fluxes.

- **Visible/UV:** Archival data of highest resolution available from the Hubble Space Telescope (HST) complement the observations López (2021). Nuclear fluxes are measured using aperture photometry of the unresolved central component by subtracting the local background from an annulus.
- **High energies:** X-ray flux measurements from Chandra, XMM-Newton, Integral, and Nustar have been collected by an extensive and careful search in the literature. Despite their lower spatial resolution, they can consistently be compared to sub-arcsec López (2021).

So, we complemented the current SED of Sombrero that was published in López (2021) and also can be found in the framework of the PARSEC project, and can be found in the works of Fernández-Ontiveros et al. (2012) Reunanen et al. (2010); Prieto (2010), with some JWST high resolution data to avoid the high absortion of our own galaxy in this part of the spectrum, as we described before and some submilimetric data from ALMA, just to show that the SED behaviour is good.

2.3. High Resolution data analysis. JWST

In subsection 2.2 we provide some context for the main data used in the SED of the Sombrero Galaxy. The data collection begins with two FITS files from the MIRI and NIRSpec instruments. To do this, we create a script in python to read the spectrum of the different fits files of the nuclei of our galaxy, plot it and select several values of the continuum (density flux, wavelenght, errors, frecuency).

2.3.1. JWST NIRS Data

The Near InfraRed Spectrograph (NIRSpec) operates over a wavelength range of 0.6 to 5 microns. A spectrograph (also sometimes called a spectrometer) is used to disperse light from an object into a spectrum. Analyzing the spectrum of an object can tell us about its physical properties, including temperature, mass, and chemical composition. The atoms and molecules in the object actually imprint lines on its spectrum that uniquely fingerprint each chemical element present and can reveal a wealth of information about physical conditions in the object. Spectroscopy and spectrometry (the sciences of interpreting these lines) are among the sharpest tools in the shed for exploring the cosmos Nasa, James Webb Space Telescope (2010a). In first place, we have two diferent files with high resolution data from the instrument NIRS (Near Infrarred Spectrograph Instrument) in two different channels:

- **First File: sombrero-nirspec-1113-p1110-g235honed.fits.** To simplify, we mentioned as ***NIRS Channel 1***. This channel from the instrument NIRS covers the wavelenght range 1.65 to 3.20 microns approximately. In this file we can found the parameters: flux density, sky and flux density error. See figure 9

- **Second File: sombrero-nirspec-1113-p1110-g395h-oned.fits.** To simplify, we mentioned as ***NIRS Channel 2***. This channel from the instrument NIRS covers the wavelenght range 3.00 to 5.50 microns approximately. In this file we can found the parameters: flux density, sky and flux density error. See figure 10

So, we used a Python script to read each FITS file, examining specific regions in the continuum and calculating the flux density for several points in each. For each measurement, we selected a central wavelength, defined a spectral window around it (sufficient to cover a small region without absorption lines), and determined minimum and maximum wavelengths within that window. We then calculated an average flux density for each measurement, along with its associated flux density error (RMS).

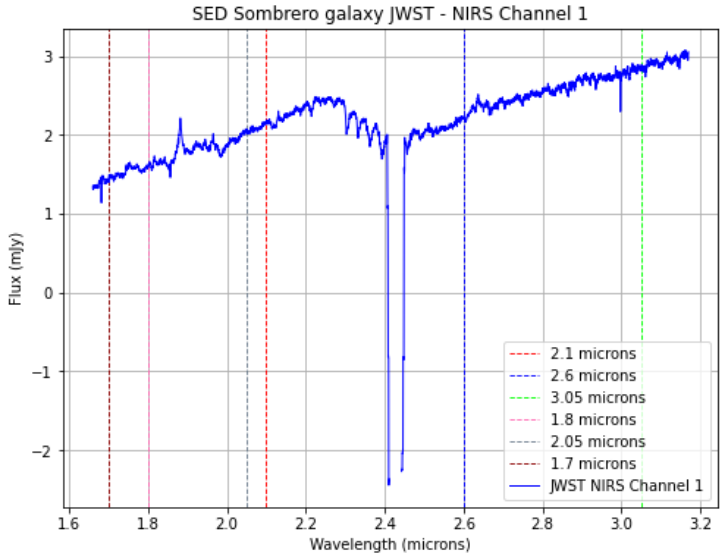

Figure 9: SED of Sombrero Galaxy using the script of pyhton to read the spectrum, measure several values in the continuum, and the final plot of the SED where we represent *Density flux in mJy* against *wavelenght in microns*. The vertical lines indicate the measurement points on the spectrum continuum. This spectrum is obtained for the first channel of NIRS, as we mentioned above as *NIRS Channel 1*.

We have to correct our data colected from NIRS with the high resolution data. To do that, we represent our NIRS data with the SED provided from López (2021) and try to pick the high resolution point which is nearest to our points in table 3. Then we calculate a ratio with the asociated fluxes between the high resolution point and our measures.

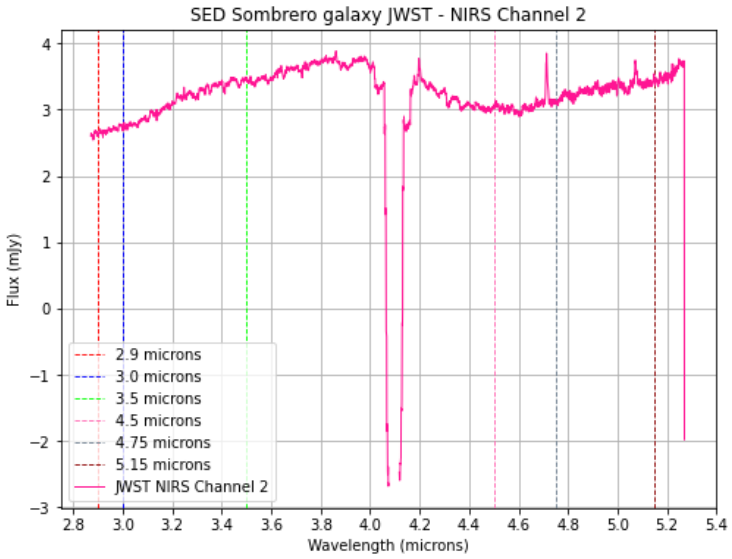

Figure 10: SED of Sombrero Galaxy using the script of pyhton to read the spectrum, measure several values in the continuum, and the final plot of the SED where we represent *Density flux in mJy* against *wavelenght in microns*. The vertical lines indicate the measurement points on the continuum. This spectrum is obtained for the second channel of NIRS, as we mentioned above as *NIRS Channel 2*.

Frecuency (Hz)	**File**	**Central Lambda** (μm)	**Av. flux (mJy)**	**Av. flux error (mJy)**
1.72×10^{14}	NIRS Channel 1	1.75	1.53	0.06
1.66×10^{14}	NIRS Channel 1	1.80	1.61	0.05
1.43×10^{14}	NIRS Channel 1	2.10	2.13	0.13
1.20×10^{14}	NIRS Channel 1	2.50	2.01	0.08
1.15×10^{14}	NIRS Channel 1	2.60	2.22	0.14
1.03×10^{14}	NIRS Channel 2	2.90	2.70	0.06
1.00×10^{14}	NIRS Channel 2	3.00	2.74	0.07
9.84×10^{13}	NIRS Channel 1	3.05	2.85	0.06
8.57×10^{13}	NIRS Channel 2	3.50	3.44	0.07
6.66×10^{13}	NIRS Channel 2	4.50	3.03	0.05
5.83×10^{13}	NIRS Channel 2	5.15	3.44	0.07

Table 3: Spectral data in tabulate format of the results of the different measurements made on NIRS Channel 1 and NIRS Channel 2. We order it from shortest to longest wavelength, also indicating the order of measurement carried out. (When we are talking about *flux* we are talking about *Density flux*. *Av* is *Average*).

Sample	**Frecuency (Hz)**	**Density Flux (mJy)**
NIRS value	1.43×10^{14}	2.13
High resolution value	1.38×10^{14}	1.00
Ratio (NIRS/ High. resolution)		**0.47**

Table 4: Calculate of the ratio to correct the NIRS values with the current high resolution data.

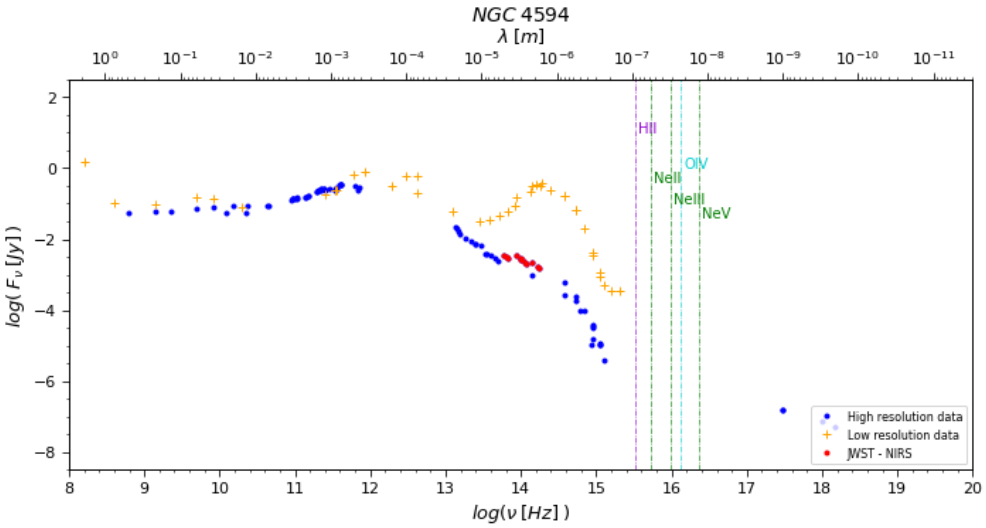

(a) SED of Sombrero Galaxy using the script of python to represent *Density flux in mJy* against *wavelenght in microns*. Our data that we show in table 3 are the red dots. Low resolution data are represented by crosses. High resolution data, are represented as blue dots. To correct them, we try to find the nearest point of our data to the high resolution points. Using python we determine that the nearest point is located in frecuency: 1.43e+14 Hz (2.13 mJy) which corresponds to the blue point with frecuency: 1.38e+14 Hz (1.00 mJy). So the ratio of fluxes are: 0.47 4. We aplied this factor to our data colected from NIRS in table 3 (Red dots).

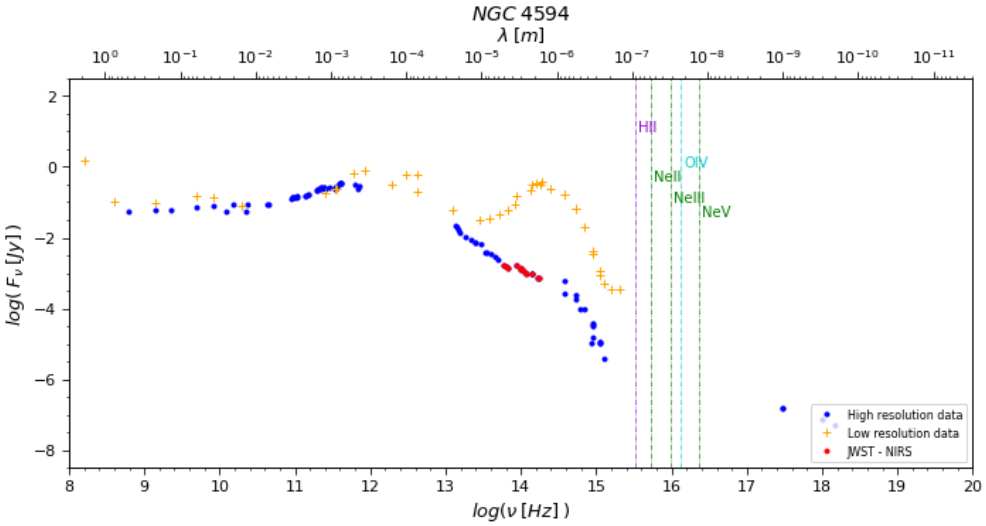

(b) SED of Sombrero Galaxy using the script of python to represent *Density flux in mJy* against *wavelenght in microns*. Here, the corretion factor is aplied to JWST NIRS data (red points) 11a.

Figure 11: Comparison of SEDs before and after correction of NIRS values.

2.3.2. JWST MIRI Data

Once we correct the data from NIRS instrument, it is time for the MIRI´s.

The Mid-Infrared Instrument (MIRI) has both a camera and a spectrograph that sees light in the mid-infrared region of the electromagnetic spectrum, with wavelengths that are longer than our eyes see. MIRI covers the wavelength range of 5 to 28 microns. Its sensitive detectors allow it to see the redshifted light of distant galaxies, newly forming stars, and faintly visible comets as well as objects in the Kuiper Belt. MIRI's camera provides wide-field, broadband imaging that continues the breathtaking astrophotography that has made Hubble so universally admired. The spectrograph enables medium-resolution spectroscopy, providing new physical details of the distant objects it observes Nasa, James Webb Space Telescope (2010b).

To do this, we use the fits provided from the *pipeline v1.11.3 and 1100.pmap*:

- **Sombrero-Miri-1d-spec-correction.fits.** To simplify, we refer to it as ***MIRI 1***. This file contains data ranging from 5 to 18 microns (mid-infrared wavelength range) and corresponds to the second calibration of the JWST. In this case, the internal radii of the annuli used to calculate the flux are slightly larger due to a different background subtraction technique, making it a more conservative option. This file was provided by David Clark Ohlson from the University of Utah.

- **Sombrero-nuc-miri-1113-p1100.fits**. To simplify, we refer to it as ***MIRI 2***. This file contains data ranging from 5 to 28 microns (mid-infrared wavelength range) and corresponds to the second calibration of the JWST. These data have been reprocessed by JWST from the MIRI instrument, representing the most recent data available. Unlike the other file, in this case the annuli have internal radii more adjusted to point sources, which reduces background presence but also results in lower flux measurements. .

So, both files correspond to the same cube of data. In fact, there are 4 channels of the MIRI instrument in the same file, unlike what we observe in the NIRS analysis.

Therefore, we decided to use values from the MIRI 2 spectrum because they represent the most recent JWST data from MIRI, cover a broader wavelength region, and the method used to obtain the fluxes is more focused on the main source (the nucleus).

The first step is to locate some regions in the continuum of the spectrum and determine the average fluxes and errors using the same method as we explained in 2.3.1.

So, acording to the conclussions obtained in figure 12 we can determine that the best option is to work with the data from MIRI 2 .

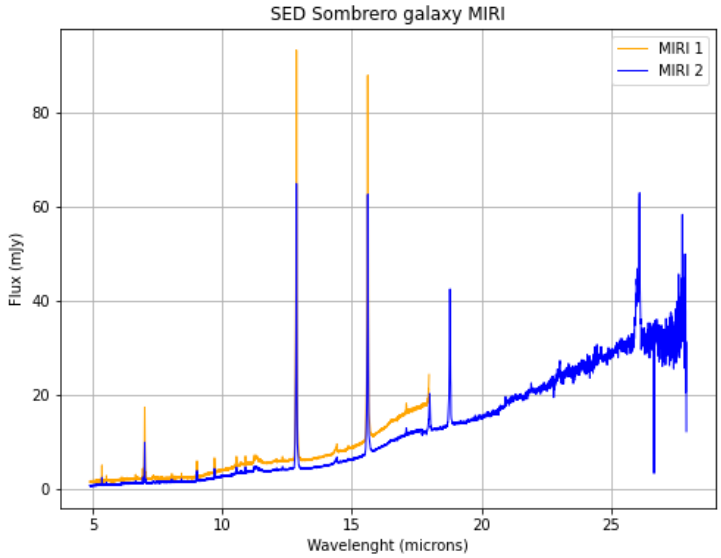

Figure 12: The SED of the Sombrero Galaxy was generated using a Python script to plot *Density flux in mJy* against *wavelength in microns*. In the plot, we can see the SED from MIRI 1 (gold data) and MIRI 2 (blue data). It appears that MIRI 2 is flatter than MIRI 1 due to the background subtraction technique mentioned above. Additionally, as the wavelength increases, the flux tends to be lower in the MIRI 2 case, which covers a broader wavelength range than MIRI 1. The final part of the MIRI 2 spectrum shows some noise..

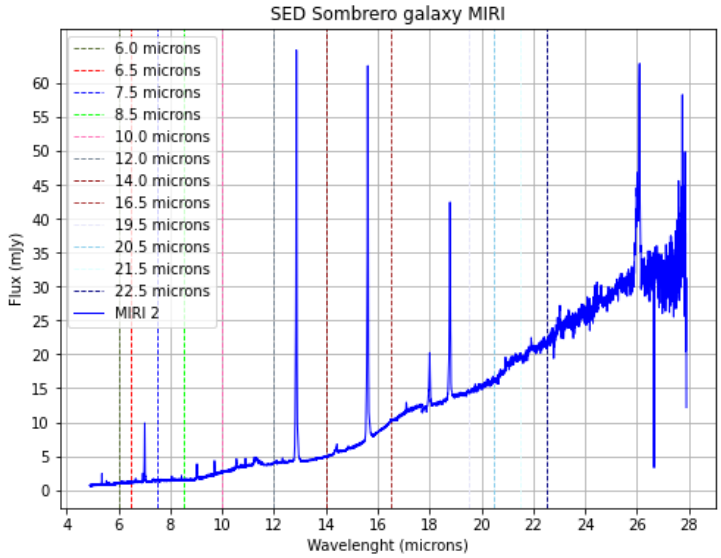

Figure 13: The SED of the Sombrero Galaxy was generated using a Python script to read the spectrum, measure several values in the continuum, and produce the final plot of the SED, where we represent *Density flux in mJy* against *wavelength in microns*. The vertical lines indicate the measurement points on the continuum. The plot shows MIRI 2 as the final choice.

Frecuency (Hz)	Lambda (μm)	Av. Flux (mJy)	RMS (mJy)
5.00×10^{13}	6.00	0.99	0.08
4.62×10^{13}	6.50	1.17	0.11
4.00×10^{13}	7.50	1.39	0.08
3.53×10^{13}	8.50	1.53	0.07
3.00×10^{13}	10.00	2.64	0.11
2.50×10^{13}	12.00	3.96	0.15
2.14×10^{13}	14.00	4.93	0.14
1.82×10^{13}	16.50	10.04	0.37
1.54×10^{13}	19.50	14.43	0.27
1.46×10^{13}	20.50	16.19	0.27
1.40×10^{13}	21.50	19.58	0.34
1.33×10^{13}	22.50	21.70	0.52

Table 5: Spectral data in tabulated format showing the results of the different measurements made on MIRI 2. The data is ordered from shortest to longest wavelength, also indicating the order in which measurements were carried out. (When referring to flux, we mean Density flux. Av stands for Average.

Following a similar strategy that was described in 2.3.1 we must correct the data with a factor. But in this case we are going to use a very high resolution data at two different wavelenghts:

- Gemini/T-ReCS 8.74 μm average value Asmus et al. (2014) with a flux of 3.70 mJy, and aperture of 0.5 arcsecs. We use this value to correct the nearby values around 9 µm from MIRI.
- VLT/VISIR 11.88 μm, 5sigma Fernández-Ontiveros et al. (2023) with a flux of 7.20 mJy, and aperture of 0.75 arcsecs. We use this value to correct the nearby values around 12 µm from MIRIs.

Sample	Frequency (Hz)	Wavelength (µm)	Density Flux (mJy)
MIRI value 1	2.50×10^{13}	12.00	3.95
High resolution value (VLT/VISIR)	2.53×10^{13}	11.85	7.20
Ratio 1 (MIRI value 1 / High. resolution value (VLT/VISIR))			**1.83**
MIRI value 2	3.53×10^{13}	8.49	1.53
High resolution value (Gemini)	3.43×10^{13}	8.74	3.70
Ratio 2 (MIRI value 2 / High. resolution value (Gemini))			**2.43**

Table 6: Calculation of the ratio to correct the MIRI values with the current high-resolution data.

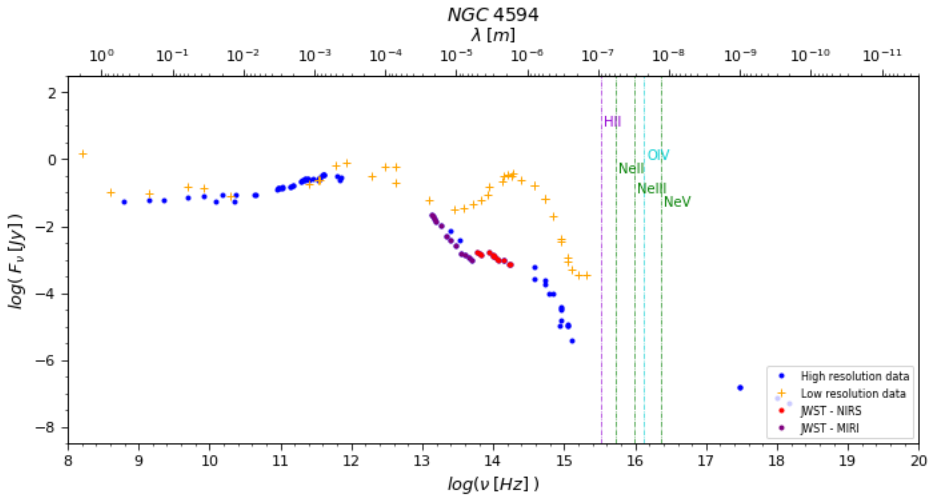

(a) SED of Sombrero Galaxy: *Density flux in mJy* against *wavelength in microns*. Our data, shown as purple dots in Table 6, are corrected using the nearest high-resolution points. For the *Gemini/T-ReCS 8.74 µm average value*, the nearest MIRI point is at 3.53e+13 Hz (1.53 mJy), resulting in a flux ratio of 2.43. This correction applies to points ranging from 0.99 to 2.64 mJy (see Table 6). For the *VLT/VISIR 11.88 µm, 5sigma*, the nearest MIRI point is at 2.50e+13 Hz (3.95 mJy), resulting in a flux ratio of 1.83. This correction applies to points ranging from 3.95 to 10.04 mJy. The remaining MIRI data points exhibit satisfactory behavior and do not require correction.

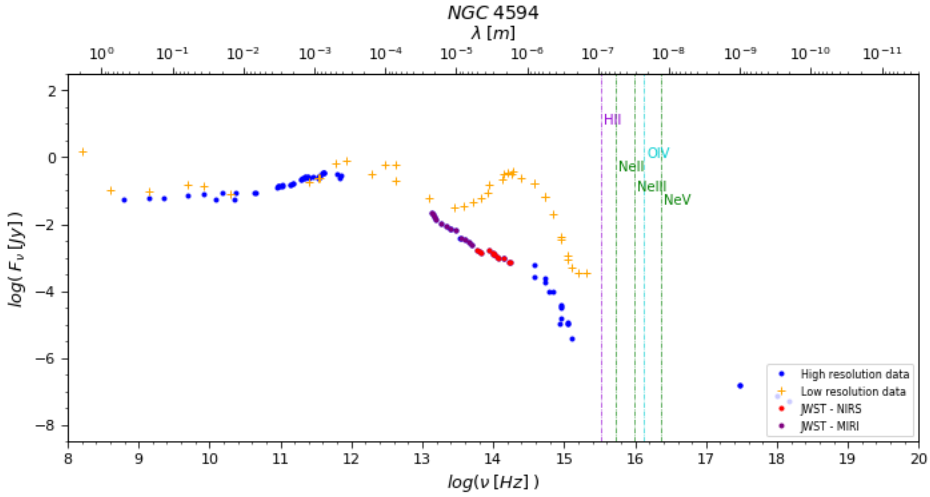

(b) SED of Sombrero Galaxy using the script of python to represent *Density flux in mJy* against *wavelenght in microns*. Here, the corretion factor is aplied to JWST MIRI data (purple points) 14a.

Figure 14: Comparison of SEDs before and after correction of MIRI values.

2.4. Radio and submilimetric data analyisis

2.4.1. Alma data

We complement the previous data with some ALMA data (submilimetric region) just to show that the data follows the model as we will see in 2.5 and in 3.

Table 7: Tabulated data of Sombrero Galaxy at different frequencies. ALMA. The data are taken between 27th of April to 16th of June, depending on frequency. The data are provided by *Tymotht Davis* from Cardiff University (UK).

Frec (Hz)	Flux (mJy)	RMS (mJy)
4.12×10^{11}	345.08	4.83
4.10×10^{11}	346.64	4.88
4.00×10^{11}	342.41	4.89
3.98×10^{11}	343.08	4.92
3.51×10^{11}	253.58	3.75
3.49×10^{11}	250.51	3.73
3.39×10^{11}	249.29	3.70
3.37×10^{11}	249.16	3.73
2.42×10^{11}	268.70	2.78
2.40×10^{11}	269.26	2.80
2.26×10^{11}	263.12	2.88
2.24×10^{11}	262.06	2.92
2.10×10^{11}	238.65	1.76
2.08×10^{11}	237.00	1.80
1.98×10^{11}	227.78	1.82
1.96×10^{11}	224.82	1.80
1.52×10^{11}	163.17	0.97
1.50×10^{11}	161.65	0.96
1.40×10^{11}	156.38	0.99
1.38×10^{11}	155.14	0.99
1.05×10^{11}	143.94	0.54
1.03×10^{11}	143.05	0.54
9.25×10^{10}	137.28	0.63
9.05×10^{10}	135.92	0.64

2.4.2. VLBI data

Finally, we added some radio data from VLBI with super high resolution. This information was extrated from a very long baseline array data at 12, 22, 44 and 88 GHz Yan et al. (2024). To introduce this data in our

work, we calculate the average of 12 and 22 GHz and its error. For 44 and 88 GHz, we calculate the average of maximun value and the minimun and the error we take the average minus the maximun value.

Sample	Frecuency (Hz)	Average Density Flux (mJy)	Av. Flux error (mJy)
VLBI (12 Ghz)	1.2×10^{10}	54.70	10.90
VLBI (22 Ghz)	2.2×10^{10}	54.10	10.80
VLBI (44 Ghz)	4.4×10^{10}	90.60	27.80
VLBI (88 Ghz)	8.8×10^{10}	120.70	58.80

Table 8: Calculate of parameters of average density flux and average density flux error Yan et al. (2024). It was measured the size of the VLBI core at 12, 22, 44 and 88 GHz in order to study its frequency dependence. At lower frequencies, which is in full agreement with previous results Hada et al. (2013). However, at higher frequencies (i.e., 88 GHz) the core size seems to desviate from this relationship. See also Yan et al. (2024)

2.5. Fitting the SED with the model

First, we can divide the model in two different contributions:

- **Jet emission.** Relativistic electrons in presence of a magnetic field (sincrotron radiation). Is represented with a 3 power law. The first one, from radio to infrarred is for the heating of the electrons. The second one, implies the cooling of the eletrons. The final one, is about the reheating of the electron by Compton efect, in the regiom between UV / X- ray, as we see in 1.3.4
- **Accretion disk.** Disk founded in BH, and follows the model explained by Sakura - Sunyaev in binaries, as we see in 1.2.2. Material sourrounding the BH is not free-falling. It is losing angular momentum so this is a sign of the posibility of a presence of a disk, by conservation of angular momentum. In this case a truncated accretion disk, that follows a pseudo-blackbody.

The high-resolution SEDs presented in previous sections have been fitted to broken power laws of the form $F \propto \nu^{-\alpha}$, with a different spectral index α in each spectral range: from the radio to the infrared, from the IR to the UV, and from UV to X-rays, as we mentioned above. These power laws become straight lines of slope $-\alpha$ when the flux/energy distributions are plotted in log-log form. The broken power laws have been forced to meet at the breaking frequency (when the frequency at which the spectral index changes). In table 9 are the input data used for the three broken power laws that define the jet contribution.

Parameter	Value	Description
ν_1	$10^{8.5}$ Hz	Lower limit of the first truncated power law
ν_2	$10^{12.5}$ Hz	Upper limit of the first truncated power law
ν_3	$10^{15.25}$ Hz	Common point for the UV and X-ray power-laws
ν_4	$10^{18.3}$ Hz	Upper limit of the second truncated power law
F_{ν_3}	$10^{-5.7}$ Jy	Flux at the common point

Table 9: Limits and common points for truncated power laws, for NGC4594 (Sombrero Galaxy). López (2021)

In adition, the main parameters which define the accretion disc are: the inner radius ($r_{\rm in}$ or x in [rin] which inplies the ratio between the innermost orbit and the gravitational radius 1.1.1, the accretion rate ($\dot{m}$, in units of $\dot{m}_{\rm edd}$), the mass of the central BH ($M_{\rm BH}$, in solar masses), normalisation factor for F_ν (unknown uncertainties), and efficiency and L_{Edd} of the BH.

Parameter	Value	Units
$r_{\rm in}$	6	[rin]
$\dot{m}$	3×10^{-5}	$\dot{M}_{\rm acc}$
$M_{\rm BH}$	10^9	$M_\odot$
Distance	9.08×10^6	Mpc
norm_flux	0.01	adim
$L_{\rm Edd}$	$1.26 \times 10^{38} \times \frac{M_{\rm BH}}{M_\odot}$	erg/s
η	0.06	adim

Table 10: Input parameters for Accretion Truncated disk, NGC4594 (Sombrero Galaxy). The dstance and Mass of the BH ($M_{\rm BH}$) are shown in table 2. The rest of parameters are from López (2021). For $r_{\rm in}$ and η values, see 1. In Ho (2008) is shown a value of 1.2×10^{39} erg/s for LINER class 2.

3. Results

Methodology applied in Section 2.3 for extracting high-resolution data of Sombrero from JWST using NIRS and MIRI instruments, along with radio and submillimeter data from ALMA and VLBI (Section 2.4), and how the data were fitted with the model (Section 2.5), will be analyzed in the following sections. In Section 3.1, we will present the plot of the entire SED and discuss the behavior of the different types of data. Then, in Section 3.1, we will analyze how well the model fits the data.

3.1. SED of NGC 4594

High resolution spectral distribution (SED) of our sample shown in 15 reveal that this object is like a radio-loud as we see in 1.3.4 for the radio synchrotron emission from a jet, until to $\nu \approx 3\times 10^{11}$ Hz. From IR to UV wavelength high resolution data shows a steep decrased (from $\nu \approx 3\times 10^{11}$ to $\nu \approx 4\times 10^{16}$ Hz). Finally between UV to X-rays, the continuum becomes less steep in high resolution data (from $\nu \approx 4\times 10^{16}$ to $\nu \approx 3\times 10^{19}$ Hz). In contrast, low resolution data show a bump in the visible range that can be a sign for stellar activity . Overall SED can be considered as a radio-loud López (2021).

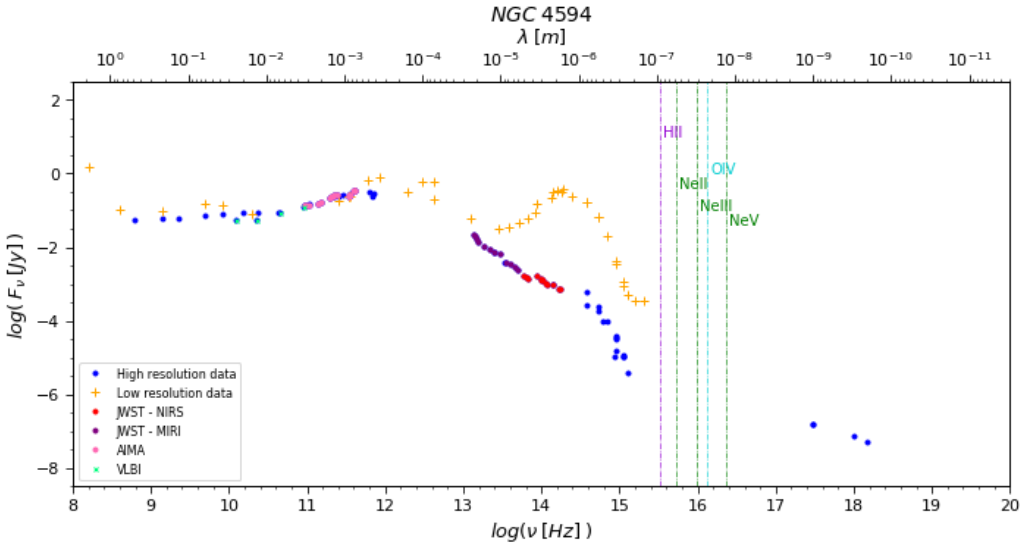

Figure 15: SED of Sombrero Galaxy in which we represent *Density flux in Jy* against *Frecuency in Hz*. The vertical lines indicate the ionization potential of some species. Also it is represented the high and low resolution data, and the data from JWST of instruments NIRS and MIRI after applied the methodology explained in 2.3. Finally we add the ALMA (submilimetric) and VLBI (radio) data that we explained in 2.4.

In addition, if we represent energy against frecuency, we can make a comparison with we were showing in figure 8. In figure 16 we can see a posible presence of a soft "big blue bump" between optical to UV that is interpreted to be as a pseudoblackbody emission from an optically thick, geometrically thin accretion disk. We will discuss this in next section.

Finally, the bolometric luminosity of the source is defined and with the Eddington Luminosity we can determine the ratio Lbol / Ledd, just for confirming this source is a LLAGN.

Luminosity	Value	Units
L_{bol}	2.55×10^{41}	erg·s
L_{Edd}	1.26×10^{47}	erg·s
$\frac{L_{bol}}{L_{Edd}}$	2.03×10^{-6}	-

Table 11: Bolometric and Eddington Luminosities and their ratio. The Bolometric luminosity is calculated using the expression asociated for it 1.2.1. The Eddington Luminosity is calculated with the expression defined in table 9. The ratio is below 10^{-3} according to what we see in section 1.3.4 and in figure 5 it is a reasonable value for this ratio. Also in Ho (2008), a Liner class 2 is shown a ratio 4.8×10^{-6}.

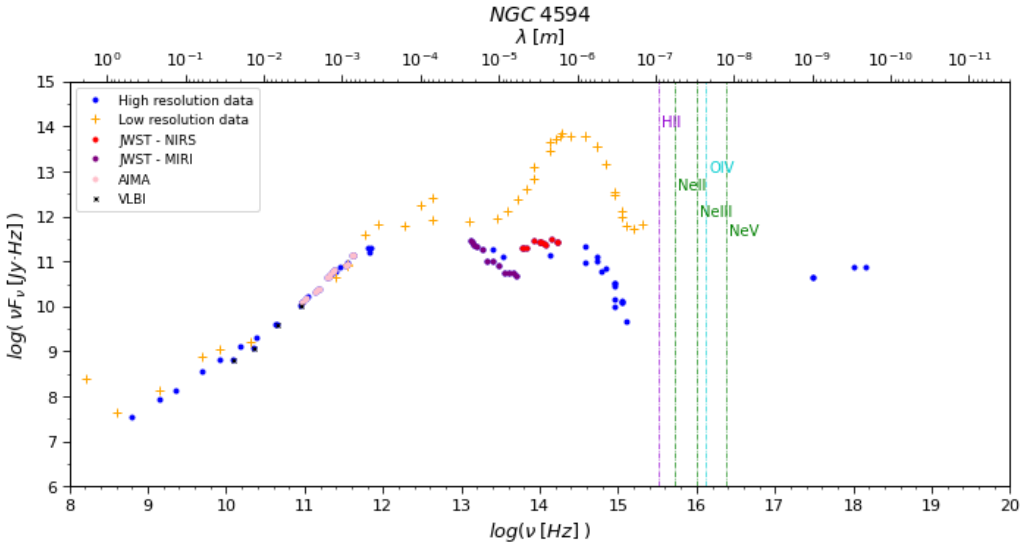

Figure 16: SED of Sombrero Galaxy in which we represent *Energy in Jy· Hz* against *Frecuency in Hz*. The vertical lines indicate the ionization potential of some species. Also it is represented the high and low resolution data, and the data from JWST from instruments NIRS and MIRI after applied the methodology explained in 2.3. Finally we add the ALMA (submilimetric) and VLBI (radio) data that we explained in 2.4.

3.2. Power law + Truncated Accretion disk

In figure 17 it is shown the modelled powerlaw plus accretion disk for our sample (NGC 4594). The vertical dashed coloured lines indicate the ionisation energy of different species as H^0 (13.6 eV), Ne^0 (21.6 eV), Ne^+ (41.0 eV), Ne^{3+} (97.1 eV) and O^{2+} (54.9 eV). The name next to each vertical dashed line corresponds to the ionic species that can be produced by photons more energetic than this threshold. The results of the power law spectral index α for radio, the optical/UV and X-ray ranges after we aplied the methodoloy explained at 2.5 and also they are in figure 17. This implies that how we explained in 2.5, the firt index is negative so the flux increased with frecuecy in the first range, and decrease in the other ranges remaining (rembember that $F \propto \nu^{-\alpha}$). See next table 12.

Power Law	Exponent (α)	Frequency Range (log ν) in Hz	E.M. range
Power law 1	-0.31	$8 < \log(\nu) < 13$	Radio
Power law 2	1.90	$13 < \log(\nu) < 16$	Visible/UV
Power law 3	0.50	$16 < \log(\nu) < 20$	X-ray

Table 12: Exponents results of the truncated power laws for NGC4594

Finally the three broken power law is added with the accretion disk model, generating a total fitting in figure 17. Also the bolometric luminosity is calculated.

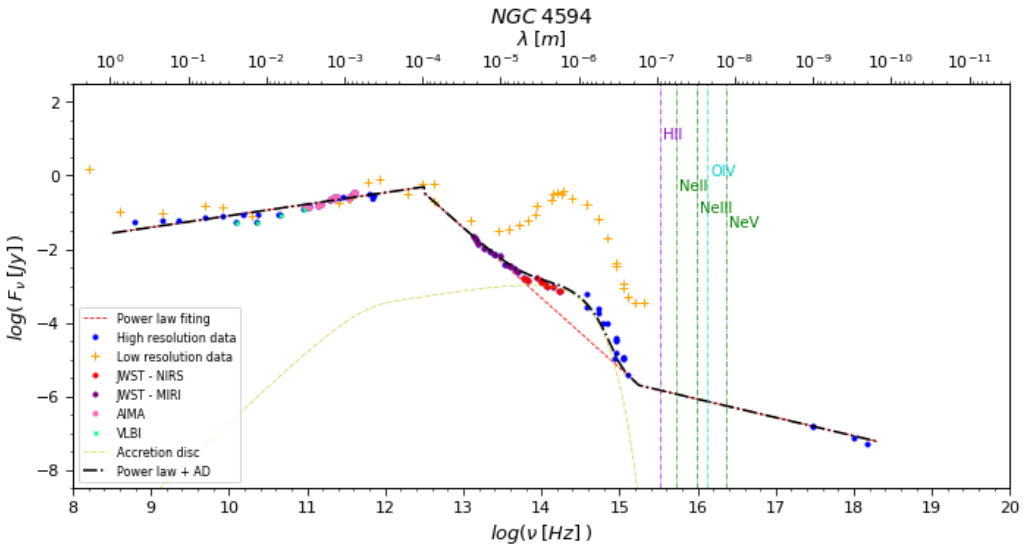

Figure 17: SED of Sombrero Galaxy in which we represent *Density flux in mJy* against *wavelenght in microns*. The vertical lines indicate the ionization potential of some species. Also it is represented the high and low resolution data, and the data from JWST of instruments NIRS and MIRI after applied the methodology explained in 2.3. Futhermore, we add the ALMA (submilimetric) and VLBI (radio) data that we explained in 2.4. Finally it is represented the three broken power-law, the accretion disk and the the powerlaw fit plus the truncated accretion disk.

4. Discussion

In this section we will comment the different results obtained in past section 3 and explain the important contribution of these very high resolution data that we were using in this work to the contribution of the posible presence of a Cold Accretion Disk in a LLAGN as NGC4594. Otherwise, we will compare with current and old works that talk of this interesting possibility in AGNs.

4.1. Ionising continuum in LLAGN and jet contribution

As we explain in section 3 our sample of a LLAGN, the continuum spectral flux is fitted with a three broken power law $F_\nu \propto \nu^{-\alpha}$ plus a truncated accretion disc. Also it follows the behaviour of a radio-loud source as we see as well in 1.3.4. Our results, supported by the high-angular resolution SED, show that the ionising continuum is consistent with a power-law interpolation from the UV to X-rays as it was predicted by López (2021). As it was described in 3.2 the fitted power laws are relatively flat in the radio ($\alpha \approx 0$) and much steeper from the IR to the UV ($\alpha \approx 2$). The X-ray data suggest that there is another turnover somewhere between the UV and the X-rays, and the continuum becomes flatter again ($\alpha \approx 0.50$). From UV/X-ray our result of the spectral index is similar to Nicholson et al. (1998) and López (2021).

4.2. The accretion disk contribution. A cold accretion disk possibility

For other hand, the spectrum of this nucleus shows a well pronounced peak at ~ 1 µm this bump is variable and therefore ascribed to the active nucleus Fernández-Ontiveros et al. (2012). The thermal-like shape could be described by an accretion disc as it is explained in Reb et al. (2018). According to our inputs parameters to accretion disk model as we see in 9 are near that it was assumed by Reb et al. (2018): a disc efficiency of $\eta = 0.1$, the inferred accretion rate is then $\dot{M} \approx 3.0 \times 10^{-6} M_\odot\,yr^{-1}$, very similar values that we used. He also claimed that if we assume as an upper limit, that all the matter entering the inner region is available to power the jet in form of energy. In this way, we define also the BH mass of our sample as it was also defined in 9 is agreed to what is in Halpern et al. (1996) and the emission is powered by accretion onto a black hole. Also we are in a sub-Eddington regime as we see in 11 acording to Nicholson et al. (1998) this may imply very low accretion rates and make NGC4594 a candidate for a 'low-state accretion disc'. Futhermore if the X-ray emission from the nucleus of NGC4594 is caused by accretion onto the $10^9\,M_\odot$ black hole implied by dynamical studies, then the luminosity is extremely sub-Eddington ($L_X = L_E < 3 \times 10^{17}$) Nicholson et al. (1998), a close value as we obtained in the results 11.

The spectral energy distribution of NGC4594 fits this model as it lacks flux in the UV Siemiginowska et al. (1996). In our sample with the very high resolution data, the lack of flux is solved and the model of an accretion disk fits in a very similar way as we can see in more luminous AGNs. This is also suggested in Maoz (2007) who argues that LLAGNs in LINERs have UV/Xray luminosity ratios similar on average to those of brighter Seyfert 1s and based on that observation he posits that thin disks extending all the way down to the radius of the innermost stable circular orbits (ISCO) persist even for LLAGNs. Another point suported by Nicholson et al. (1998) so in LINERs as Sombrero, the X-ray luminosity is also consistent with the nucleus behaving like a downsized version of an AGN and also no Fe Kα line, which may indicate that there is no standard, thin accretion disc, as well as we found in Ho (2008).

Futhermore, Schlafly & Finkbeiner (2011) follows a similar idea that a significant fraction of LLAGNs near a SMBH should fall into a cold Accretion Disk (AD) regime. The narrow emission lines of these sources are likely powered by a hard continuum, and it suggests that this type of source could be fitted by a cold AD.

Additionally, López (2021) suggests that NGC 4594 exhibits a thermal component attributed to a truncated accretion disk with very low accretion rates. This cold disk peaks at approximately 1 µm, as confirmed by our results. In the context of LLAGN, it is proposed that accretion disks, if present, are significantly colder, typically truncated at $r_{\rm in} \sim 10 - 50 r_g$ with accretion rates $\dot{m} \sim 10^{-5} - 10^{-3} \dot{m}_{\rm edd}$.

4.3. Advection Dominated Acrretion Flows Models

Another posibility to explain our results is the ADAF model (Advection Dominated Acrretion Flows) as we see in the first part of our work. This accretion processes in LLAGN occurs when the cooling time-scale becomes longer than the accretion time-scale, so that most of the dissipatively liberated energy is advected inward with the accreted gas rather than being radiated Nicholson et al. (1998). In adittion, Nemmen et al. (2014) adopt a coupled accretion-jet model comprising an inner advection-dominated accretion (ADAF) and an outer standard thin disk in different LLAGNs sample and one of this was Sombrero galaxy (our sample).

The emission from a thin accretion disk whose inner radius is truncated at the outer radius of the ADAF. The accretion may begin as a standard thin disk but somehow at a certain transition radius it gradually switches from a cold to a hot ADAF model. The inner part of the accretion flow is in the form of an ADAF which is a hot, geometrically thick, optically thin two-temperature accretion flow, which has low radiative efficiency.

So if we see figure 18 we can see the bump in IR but not the second one in our results shown in figure 17 we can see that for our high resolution data this bump does not fit in such way, because in our results the Visible/Uv region is steeper than in this figure. So we conclude that ADAF model is not the best option due to the recent very high resolution data we used in our work.

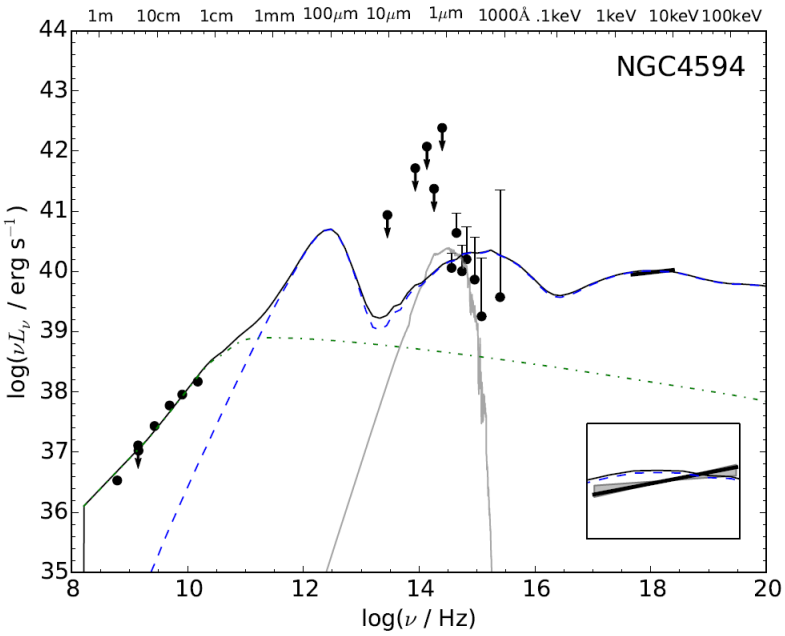

Figure 18: SED of Sombrero Galaxy in which it is represented *Energy in Jy · Hz* against *wavelenght in microns* of Sombrero Galaxy with the ADAF model Nemmen et al. (2014)

5. Conclusions

In this study we have investigated the spectral energy distribution (SED) of the object NGC 4594 (Sombrero galaxy) a LLAGN and LINER. Based on existing data, we have carried out an analysis of new very high resolution data provided by JWST in its NIRSpec and MIRI instruments in the infrared wavelength ranges, where there is currently a lack of data in this class of objects so not very bright. We complement these data with data from ALMA in the submillimeter region and from VLBI, in radio to verify the good behavior of our object when fitting it with a power law and a disk model.

Therefore, we reach the following conclusions:

- **Radio-loud source:** Our results reveal that NGC 4594 exhibits typical features of a radio-loud object up to frequencies of approximately 3×10^{11} Hz, where synchrotron radio emission is observed, consistent with the presence of a jet.
- **Fitting with a three broken power law plus accretion disk:** The Spectral Energy Distribution could be successfully modeled by a power-law interpolation of the high angular resolution spectral flux data, plus a truncated disk component. The contribution of the disk is clearly visible in our candidate, NGC 4594, with a clear thermal component in its SED.
- **Presence of a 'Cold Accretion Disk' and LLAGN Behavior:** From infrared to ultraviolet wavelengths, the high-resolution data show a steep decline in the spectral flux, followed by a region where the spectrum flattens between ultraviolet and X-rays, before decreasing again at higher frequencies. These characteristics suggest the presence of a truncated and possibly cold accretion disk, which can explain the observed behavior in the UV-X-ray region. The presence of a possible "big blue bump" between optical and UV, as well as a "big red bump" related to the mid-infrared excess, supports the interpretation of a pseudo-blackbody emission from an optically thick, geometrically thin accretion disk. This disk appears to be truncated in the inner regions, consistent with models of cold accretion disks. Unlike typical LLAGNs, which often lack a clear big blue bump and exhibit a flat SED in the far-IR, NGC 4594 shows distinct evidence of a cold accretion disk. The JWST data have allowed us to identify the presence of this structure, which was not possible with previous observations.
- **ADAF model possibility:** Comparing with other models such as advection-dominated accretion flows (ADAFs), our high-resolution data do not exhibit the expected behavior for an ADAF model in the UV region, where the slope of the spectrum is steeper than expected for an ADAF. This supports the idea that a truncated cold accretion disk model is more appropriate to explain the observed SED in NGC 4594, providing better agreement with current observations.

In summary, our results suggest the presence of a truncated cold accretion disk in NGC 4594, shifted towards longer wavelengths, as discussed in our work, since our object is a Sub-Eddington candidate whose disk is not standard like that of a quasar or Seyfert.

References

Antonucci R., 1993, ARA&A, 31, 473

Asmus D., Hönig S. F., Gandhi P., Smette A., Duschl W. J., 2014, MNRAS, 439, 1648

Bajaja E., Dettmar R. J., Hummel E., Wielebinski R., 1988, A&A, 202, 35

Barth A. J., Ho L. C., Filippenko A. V., Rix H.-W., Sargent W. L. W., 2001, ApJ, 546, 205

Bendo G. J., et al., 2006, ApJ, 645, 134

Chen K., Halpern J., 1989a, News Letter of the Astronomical Society of New York, 3, 19

Chen K., Halpern J. P., 1989b, ApJ, 344, 115

Done C., Gierliński M., Sobolewska M., Schurch N., 2007, in Ho L. C., Wang J. W., eds, Astronomical Society of the Pacific Conference Series Vol. 373, The Central Engine of Active Galactic Nuclei. p. 121 (arXiv:astro-ph/0703449), doi:10.48550/arXiv.astro-ph/0703449

Elvis M., et al., 1994, ApJS, 95, 1

Faber S. M., Balick B., Gallagher J. S., Knapp G. R., 1977, ApJ, 214, 383

Fernández-Ontiveros J. A., Prieto M. A., Acosta-Pulido J. A., Montes M., 2012, in Journal of Physics Conference Series. IOP, p. 012006 (arXiv:1206.0777), doi:10.1088/1742-6596/372/1/012006

Fernández-Ontiveros J. A., López-López X., Prieto A., 2023, A&A, 670, A22

González-Martín O., Masegosa J., Márquez I., Guerrero M. A., Dultzin-Hacyan D., 2006, A&A, 460, 45

Hada K., Doi A., Nagai H., Inoue M., Honma M., Giroletti M., Giovannini G., 2013, ApJ, 779, 6

Halpern J. P., Eracleous M., 1994, ApJ, 433, L17

Halpern J. P., Eracleous M., Filippenko A. V., Chen K., 1996, ApJ, 464, 704

Heckman T. M., 1980, Highlights of Astronomy, 5, 185

Ho L. C., 2002, in Green R. F., Khachikian E. Y., Sanders D. B., eds, Astronomical Society of the Pacific Conference Series Vol. 284, IAU Colloq. 184: AGN Surveys. p. 13 (arXiv:astro-ph/0110438), doi:10.48550/arXiv.astro-ph/0110438

Ho L. C., 2008, ARA&A, 46, 475

Ho L. C., Peng C. Y., 2001, ApJ, 555, 650

Ho L. C., Rudnick G., Rix H.-W., Shields J. C., McIntosh D. H., Filippenko A. V., Sargent W. L. W., Eracleous M., 2000, ApJ, 541, 120

Hummel E., van der Hulst J. M., Dickey J. M., 1984, A&A, 134, 207

Inoue H., Terashima Y., Ho L. C., 2007, in Karas V., Matt G., eds, Vol. 238, Black Holes from Stars to Galaxies – Across the Range of Masses. pp 385–386, doi:10.1017/S1743921307005571

Jensen J. B., Tonry J. L., Barris B. J., Thompson R. I., Liu M. C., Rieke M. J., Ajhar E. A., Blakeslee J. P., 2003, ApJ, 583, 712

Kato S., 1998, Black-hole accretion disks

Kinkhabwala A., et al., 2002, ApJ, 575, 732

Kormendy J., Ho L. C., 2013, arXiv e-prints, p. arXiv:1308.6483

Laor A., 2003, ApJ, 590, 86

Lawrence A., 2005, MNRAS, 363, 57

Lawrence A., Elvis M., 1982, ApJ, 256, 410

Livio M., Ogilvie G. I., Pringle J. E., 1999, ApJ, 512, 100

López X. L., 2021, Master's thesis, Universidad de La Laguna, http://riull.ull.es/xmlui/handle/915/23099

Maoz D., 2007, MNRAS, 377, 1696

Narayan R., Yi I., 1995, ApJ, 444, 231

Nasa, James Webb Space Telescope M. i., 2010b, MID-INFRARED INSTRUMENT (MIRI), Nasa

Nasa, James Webb Space Telescope N. i., 2010a, NEAR INFRARED SPECTROGRAPH (NIRSPEC), Nasa

Nemmen R. S., Storchi-Bergmann T., Eracleous M., 2014, MNRAS, 438, 2804

Netzer H., 2013, The Physics and Evolution of Active Galactic Nuclei

Nicholson K. L., Reichert G. A., Mason K. O., Puchnarewicz E. M., Ho L. C., Shields J. C., Filippenko A. V., 1998, MNRAS, 300, 893

Peterson B. M., Ferland G. J., 1997, The Structure of the Broad-Line Region in Well-Studied AGNs, Technical Report, Ohio State Univ. Columbus, OH United States

Petre R., Mushotzky R. F., Serlemitsos P. J., Jahoda K., Marshall F. E., 1993, ApJ, 418, 644

Pogge R. W., Maoz D., Ho L. C., Eracleous M., 2000, ApJ, 532, 323

Prieto A., 2010, Genuine spectral energy distribution of active galactic nuclei, IAC Talks, Astronomy and Astrophysics Seminars from the Instituto de Astrofísica de Canarias, id.99

Ptak A., Yaqoob T., Mushotzky R., Serlemitsos P., Griffiths R., 1998, ApJ, 501, L37

Reb L., Fernández-Ontiveros J. A., Prieto M. A., Dolag K., 2018, MNRAS, 478, L122

Rees M. J., 1982, in Heeschen D. S., Wade C. M., eds, Vol. 97, Extragalactic Radio Sources. pp 211–221

Reunanen J., Prieto M. A., Siebenmorgen R., 2010, MNRAS, 402, 879

Schlafly E., Finkbeiner D. P., 2011, in American Astronomical Society Meeting Abstracts #217. p. 434.42

Shakura N. I., Sunyaev R. A., 1973, A&A, 24, 337

Shields G. A., 1978, Nature, 272, 706

Shields J. C., Rix H.-W., McIntosh D. H., Ho L. C., Rudnick G., Filippenko A. V., Sargent W. L. W., Sarzi M., 2000, ApJ, 534, L27

Shields J. C., Sabra B. M., Ho L. C., Barth A. J., Filippenko A. V., 2002, in Crenshaw D. M., Kraemer S. B., George I. M., eds, Astronomical Society of the Pacific Conference Series Vol. 255, Mass Outflow in Active Galactic Nuclei: New Perspectives. p. 105

Siemiginowska A., Czerny B., Kostyunin V., 1996, ApJ, 458, 491

Starling R. L. C., Page M. J., Branduardi-Raymont G., Breeveld A. A., Soria R., Wu K., 2005, MNRAS, 356, 727

Terashima Y., Ho L. C., Ptak A. F., 2000, ApJ, 539, 161

Urry C. M., Padovani P., 1995, PASP, 107, 803

Vanden Berk D. E., et al., 2001, AJ, 122, 549

Veilleux S., Osterbrock D. E., 1987, in Lonsdale Persson C. J., ed., NASA Conference Publication Vol. 2466, NASA Conference Publication. pp 737–740

Verdoes Kleijn G. A., van der Marel R. P., Noel-Storr J., 2006, AJ, 131, 1961

Walsh J. L., 2011, PhD thesis, University of California, Irvine

Yan X., Lu R.-S., Jiang W., Krichbaum T. P., Xie F.-G., Shen Z.-Q., 2024, ApJ, 965, 128

Yuan F., 2007, in Ho L. C., Wang J. W., eds, Astronomical Society of the Pacific Conference Series Vol. 373, The Central Engine of Active Galactic Nuclei. p. 95 (arXiv:astro-ph/0701638), doi:10.48550/arXiv.astro-ph/0701638

van Houten C. J., 1961, PhD thesis, Leiden Observatory